# Iron isotopic evolution during fractional crystallization of the uppermost Bushveld Complex layered mafic intrusion

**Laura D. Bilenker[1]†, Jill A. VanTongeren[2], Craig C. Lundstrom[3], and Adam C. Simon[1]**

[1]Department of Earth and Environmental Sciences, University of Michigan, 2534 C.C. Little Building, 1100 N. University Ave., Ann Arbor, MI 48109-1005 USA

[2]Department of Earth and Planetary Sciences, Rutgers University, Wright Geological Laboratory 343, 610 Taylor Rd., Piscataway, NJ 08854-8066 USA

[3]Department of Geology, University of Illinois, Urbana-Champaign, 152 Computer Applications Building, 605 E. Springfield Ave., Champaign, IL 61820 USA

Corresponding author: Laura Bilenker (bilenker@umich.edu)

†Current address: Pacific Centre for Isotopic and Geochemical Research, Department of Earth, Ocean, and Atmospheric Sciences, 2020-2207 Main Mall, University of British Columbia, Vancouver, B.C. V6T 1Z4 Canada

**Key Points:**

- Whole rock and magnetite separates from the uppermost portion of the Bushveld Complex were analyzed for their Fe isotope compositions.
- We find no systematic variation in whole rock or magnetite Fe isotope ratios with stratigraphic height.
- 85% crystallization of a dry tholeiitic multiply-saturated magma does not significantly fractionate Fe isotopes.

## Abstract

We present $\delta^{56}Fe$ ($^{56}Fe/^{54}Fe$ relative to standard IRMM-014) data from whole rock and magnetite of the Upper and Upper Main Zones (UUMZ) of the Bushveld Complex. With it, we assess the role of fractional crystallization in controlling the Fe isotopic evolution of a mafic magma. The UUMZ evolved by fractional crystallization of a dry tholeiitic magma to produce gabbros and diorites with cumulus magnetite and fayalitic olivine. Despite previous experimental work indicating a potential for magnetite crystallization to drastically change magma $\delta^{56}Fe$, we observe no change in whole rock $\delta^{56}Fe$ above and below magnetite saturation. We also observe no systematic change in whole rock $\delta^{56}Fe$ with increasing stratigraphic height, and only a small variation in $\delta^{56}Fe$ in magnetite separates above magnetite saturation. Whole rock $\delta^{56}Fe$ (errors twice standard deviation, $\pm 2\sigma$) throughout the UUMZ ranges from -0.01 ±0.03‰ to 0.21 ±0.09‰ ($\delta^{56}Fe_{averageWR}$ = 0.10 ±0.09‰; n=21, isotopically light outlier: $\delta^{56}Fe_{WR}$ = -0.15‰), and magnetites range from 0.28 ±0.04‰ to 0.86 ±0.07‰ ($\delta^{56}Fe_{averageMgt}$ = 0.50 ±0.15‰; n=20), similar to values previously reported for other layered intrusions. We compare our measured $\delta^{56}Fe_{WR}$ to a model that incorporates the changing normative mineralogy, calculated temperatures, and published fractionation factors of Fe-bearing phases throughout the UUMZ and produces $\delta^{56}Fe_{WR}$ values that evolve only in response to fractional crystallization. Our results show that the Fe isotopic composition of a multiply-saturated (multiple phases on the liquidus) magma is unlikely to change significantly during fractional crystallization of magnetite due to the competing fractionation of other Fe-bearing cumulus phases.


## 1 Introduction

Significant variations of stable Fe isotope ratios are predicted to occur under magmatic/magmatic-hydrothermal conditions (i.e., high T, P) [e.g., *Shahar et al.*, 2008].

Proposed magmatic processes leading to isotopic fractionation include fractional crystallization [e.g., *Schuessler et al.,* 2007; *Schuessler et al.,* 2009; *Teng et al.,* 2008], fluid exsolution [*Poitrasson and Freydier,* 2005; *Heimann et al.,* 2008; *Telus et al.,* 2012], changes in oxygen fugacity ($fO_2$) [*Williams et al.,* 2005; *Sossi et al.,* 2012, *Foden et al.,* 2015], bonding environment [e.g., *Dauphas et al.,* 2014; *Sossi et al.* 2017] and thermal gradients [*Lundstrom et al.,* 2009; *Huang et al.,* 2010; *Zambardi et al.,* 2014].

Several of these processes are likely at play in a magmatic/magmatic-hydrothermal system during and after its formation, and the Fe isotope signature of whole rock samples will reflect all of them. Iron isotope fractionation factors among mineral, melt, and aqueous fluid have been determined by analyses of natural and experimental samples, as well as estimated theoretically. Using these published fractionation factors, it is possible to combine these data with field, petrological, and additional geochemical observations to elucidate the contributions of individual processes to the measured Fe isotope ratio of a sample. Isolating processes by studying a controlled experimental or closed natural system can help advance our understanding of Fe isotope fractionation at magmatic/magmatic-hydrothermal conditions and in turn improve our ability to interpret the geologic history of a deposit or intrusion based upon the Fe isotope composition of rocks and minerals.

*Schuessler et al.* [2007], *Shahar et al.* [2008], and *Sossi and O'Neill* [2017] are the only published experimental studies to date conducted at conditions relevant to igneous systems. This is significant because such high-temperature experimental studies allow for direct measurement of isotope fractionation factors at conditions approaching equilibrium between crystals and liquid. The studies of *Schuessler et al.* [2007] and *Shahar et al.* [2008] demonstrated that Fe isotopes should fractionate in igneous systems due to the crystallization of individual mineral

68 phases as well as due to magmatic redox processes. In the first published high-temperature
69 experimental Fe isotope fractionation study, *Schuessler et al.* [2007] found that pyrrhotite ($Fe_{1-x}S$)
70 preferentially incorporates isotopically light Fe by an average fractionation factor
71 ($\Delta^{56}Fe_{pyrrhotite\text{-}melt}$) of about 0.35‰ relative to a silicic melt with ~62% $Fe^{3+}$ between 800°C and
72 1000°C. Similarly, *Shahar et al*. [2008] performed experiments that demonstrated that magnetite
73 is isotopically heavy relative to fayalite and quantified the amount of equilibrium fractionation
74 between the two phases over a range of magmatic/magmatic-hydrothermal temperatures. The
75 results of these studies are consistent with expectations based upon the fact that the Fe in the
76 pyrrhotite and fayalite structures is $Fe^{2+}$ while the Fe in magnetite is mostly $Fe^{3+}$, although other
77 factors such as ligand strength (e.g., Fe is bonded to S in pyrrhotite) also play a role.
78 Theoretical studies predicted this correlation between higher valence and heavier isotopic
79 composition [e.g., *Polyakov and Mineev*, 2000; *Polyakov et al.*, 2007], and the force constant
80 measurements and subsequent modeling of *Dauphas et al.* [2014] is also consistent with Fe
81 isotope fractionation being connected to redox and bonding environment. In the most recent
82 experimental study on stable Fe isotope fractionation in magmatic systems, *Sossi and O'Neill.*
83 [2017] performed piston-cylinder experiments between a $FeCl_2$-bearing fluid and various
84 minerals within which $Fe^{2+}$ exists in VIII, VI, IV coordination. Magnetite, which contains $Fe^{3+}$ in
85 addition to $Fe^{2+}$ and therefore has Fe in a mix of VI and IV coordination, was the isotopically
86 heaviest mineral in the study. Their work provides further evidence that coordination number and
87 bond length control fractionation.
88 The above experimental data are also consistent with field-based observations, such as
89 those of *Sossi et al.* [2012]. Iron isotope data from the Red Hill sill supports a hypothesis that
90 couples redox and fractional crystallization. *Sossi et al.* [2012] sampled stratigraphically

91 throughout the 420 m thick sill in Tasmania, which is thought to have formed by a single
92 intrusive event. The system was assumed closed to $O_2$ and experienced fractional crystallization.
93 The whole rock data for the Red Hill sill show a trend toward isotopically heavy compositions
94 early during the crystallization of pyroxene, which peak at magnetite saturation, and then
95 become systematically lighter during magnetite crystallization (i.e., isotopically light Fe is
96 removed from the melt by pyroxene and isotopically heavy Fe is removed from the melt by
97 magnetite).

98 *Teng et al.* [2008] was the first study to present evidence in natural rocks for Fe isotope
99 fractionation during fractional crystallization. By analyzing whole rocks and mineral separates
100 from Kilauea Iki, Hawaii, USA, they showed that olivine, which preferentially incorporates $Fe^{2+}$,
101 is isotopically lighter than a co-existing melt with respect to Fe isotopes. Later work on Kilauea
102 Iki olivine phenocrysts combined Mg isotope measurements and Mg/Fe ratios with Fe isotope
103 data [*Teng et al.,* 2011]. The resulting modeling suggested that the olivine grains might be
104 isotopically light with respect to Fe due to the ability of lighter isotopes to diffuse faster than
105 heavier isotopes during magmatic differentiation. *Schuessler et al.* [2009] also focused on natural
106 samples during their study on the dacitic and rhyolitic eruption products of Hekla volcano in
107 Iceland. The Fe isotope compositions of the rhyolite samples were isotopically heavy compared
108 to the dacite samples. Due to a lack of evidence for extensive fluid exsolution, the authors
109 concluded that the difference in isotopic composition between the two groups of samples
110 reflected fractional crystallization as the magma evolved from a dacite to a rhyolite; however no
111 fractionating phase assemblage was specified to make this a quantitative model. Indeed, the
112 original premise of *Poitrasson and Freydier* [2005] that there exists a strong hyperbolic increase
113 toward heavier Fe isotopes in higher silica igneous rocks is clearly supported by the global

114 database (e.g., *Heimann et al.,* 2008; *Schuessler et al.,* 2009; *Teng et al.,* 2011; *Sossi et al.,* 2012;
115 *Foden et al.,* 2015).

116 1.1 Iron isotopes in layered mafic intrusions

117 Despite these important studies, the mechanisms that control Fe isotope fractionation are
118 still being actively investigated [e.g., *Young et al.,* 2015], and little work has been done to apply
119 Fe isotopes as a tool for studying the processes that form layered mafic intrusions [*Schoenberg et*
120 *al.,* 2009; *Chen et al.,* 2014; *Liu et al.* 2014]. Layered mafic intrusions are fossilized shallow
121 crustal magma chambers found worldwide and in many cases contain economic amounts of
122 platinum group elements and chromite.

123 Among the layered mafic intrusions exposed today, the ~2.06 Ga Bushveld Complex
124 located in the Kaapvaal craton is the largest. Within the Bushveld Complex, the mafic-ultramafic
125 Rustenberg Layered Suite (RLS) was likely formed from four major pulses of magma, and the
126 uppermost ~2.5 km of the 8-9 km thick intrusion are represented by the Upper and Upper Main
127 Zones (UUMZ) (Fig 1). On the basis of major element, trace element, and isotopic geochemical
128 trends, the rocks of the UUMZ are thought to reflect the crystallization products from the final
129 pulse of magma into the chamber [e.g., *Kruger et al.,* 1987; *Tegner et al.,* 2006; *VanTongeren et*
130 *al.,* 2010; *VanTongeren and Mathez*, 2013] with little to no volumetrically significant additional
131 input of new magma or crustal contamination above this level. This makes the well-characterized
132 RLS the ideal location in which to further investigate the evolution of Fe isotopes during
133 fractional crystallization in a multiply saturated system (multiple phases on the liquidus at a
134 given temperature) with and without magnetite.

135 Above a 3 m thick orthopyroxenite layer, the Pyroxenite Marker, the UUMZ is
136 characterized by an evolving phase assemblage of pyroxene (px) + plagioclase (plag) → px +

137 plag + magnetite (mgt) → px + plag + mgt + fayalitic olivine (ol) → px + plag + mgt + ol +
138 apatite (ap). For the first ~1500 m, opx and cpx co-exist, but opx disappears shortly after
139 magnetite saturation. *VanTongeren et al.* [2010] showed that the cumulus mineral compositions
140 and phase assemblages in the UUMZ evolved by fractional crystallization from a single parent
141 magma composition from the Pyroxenite Marker to the roof of the intrusion (Fig. 1, Fig. S1).
142 The lower ~500 m of the UUMZ is a two-pyroxene gabbro with approximately 40%
143 pyroxene and 60% plagioclase. At ~2850 m cumulus magnetite joins the stratigraphy and is
144 typically present as minor (2-10 modal %) disseminated grains throughout the gabbroic rocks.
145 Below 2850 m, there is a small amount of intercumulus magnetite present. In addition, the Upper
146 Zone is known for its 21 layers of nearly monomineralic magnetitite. Magnetitite layers range in
147 thickness from 10s of cm, to >3 m for the Main Magnetite Layer, however local variations in
148 thickness do occur. For example, the uppermost magnetite layer (Seam 21) in the eastern
149 Bushveld reaches up to 60 m thick in certain locations. Fayalitic olivine becomes a liquidus
150 phase at ~3500 m, forming an initial troctolite horizon before the stratigraphy becomes
151 dominated by ol-diorites for the remainder of the crystallization sequence. In this study, we
152 report Fe isotope data from whole rocks and magnetite separates throughout the stratigraphy of
153 the UUMZ in the eastern Bushveld Complex to investigate the effect of magmatic differentiation
154 on the isotopic evolution of the magma in a well-characterized, large intrusion.
155 Considering the available published data on Fe isotope fractionation at relevant magmatic
156 conditions, one would predict that whole rock isotopic compositions of samples near the bottom
157 of the UUMZ (i.e., prior to magnetite saturation with abundant $Fe^{2+}$-rich phases) would be
158 isotopically lighter than those near the roof. Assuming crystallizing phases are separated
159 instantaneously from the melt, around the stratigraphic level of magnetite saturation, we would

160 expect the whole rock Fe isotope composition to peak at its heaviest and become lighter
161 stratigraphically upward. Deviations from, or consistency with, this hypothesized pattern will
162 provide insight into the magmatic processes that formed the layered rocks of UUMZ.
163
164 **2 Estimating Fe Isotope Evolution throughout the UUMZ During Fractional**
165 **Crystallization**
166 We construct a simple model that incorporates the normative abundances of all cumulus
167 phases throughout the UUMZ, their FeO contents, and their fractionation factors, in order to
168 investigate the effect of fractional crystallization on the Fe isotope composition of the bulk rocks
169 throughout the UUMZ. The Fe isotope composition of the UUMZ is likely controlled by the
170 phase containing the largest proportion of the Fe in the rocks: magnetite. In addition, published
171 fractionation factors imply a large fractionation of Fe isotopes between magnetite and melt. Each
172 of the other Fe-bearing phases present (ol, opx, cpx, plag) will also have a varying effect.
173 Therefore, it is reasonable to expect that the Fe isotope systematics of the UUMZ will reflect
174 fractional crystallization, and accumulation.
175 Our model of the UUMZ assumes perfect fractional crystallization; i.e., a controlled
176 amount of liquid crystallizes at each step (5% of the initial liquid present, not 5% of the liquid
177 present at each step). The model stops at 15% liquid remaining, at which point the residual
178 magma is erupted to the surface to form portions of the Rooiberg Group lavas and/or Rashoop
179 Granophyres. This was proposed by *VanTongeren et al*. [2010] on the basis of MELTS phase
180 equilibria and further supported by trace element equilibrium between the uppermost cumulates
181 and the Rooiberg lavas [e.g. *VanTongeren and Mathez,* 2012]. Values incorporated into the

model for percent liquid remaining are correlated to the stratigraphic height in the UUMZ according to the following relationship:

$$\text{Liquid remaining (\%)} = 15 + 100*(4625 - d)/2850 \quad \text{(eqn. 1)}$$

where d represents the stratigraphic depth in meters above the Merensky Reef in the eastern Bushveld. The term 100*(4625– d) is then divided by the original thickness of the UUMZ magma column prior to eruption. The Pyroxenite Marker defines the base of the UUMZ at 2200 m (100% liquid remaining). The roof of the UUMZ is at 4625 m (15% liquid remaining). The total original thickness of magma present in the UUMZ is 2850 m, which takes into account the total current UUMZ thickness of 2425 m plus the 425 m of magma estimated to be lost (15% of the original; e.g. VanTongeren et al., 2010).

### 2.1 Modeling the evolution of $\delta^{56}Fe$

The isotopic composition of a system (i.e., whole rock) can be calculated from the sum of the isotopic values of each component (i.e., each mineral) weighted by their relative abundances. The fractionation of Fe isotopes throughout the UUMZ stratigraphy was modeled by the mass balance equations:

$$\delta^{56}Fe_{liquidY} = X_{liquid(Y-1)} * \delta^{56}Fe_{liquid(Y-1)} - X_{WR(Y-1)} * \delta^{56}Fe_{WR(Y-1)} \quad \text{(eqn. 2)}$$

$$\delta^{56}Fe_{WR} = \delta^{56}Fe_{phase1} * X_{phase1} * FeO_{phase1}/FeO_{WR} + \delta^{56}Fe_{phase2} * X_{phase2} * FeO_{phase1}/FeO_{WR} + \ldots + \delta^{56}Fe_{phaseX} * X_{phaseX} * FeO_{phase1}/FeO_{WR} \quad \text{(eqn. 3)}$$

where Y is the current step within the evolution of the magma and Y-1 represents the previous step. In equation 2, $X_{liquid}$ is the proportion of liquid remaining and $X_{WR}$ is the mass fraction of whole rock that is removed (i.e., crystallized) at each step. In equation 3, X represents the normalized modal abundance of an individual phase within the whole rock and $FeO_{phase}/FeO_{WR}$

205 represents the fraction of FeO that the phase contributes to the whole rock value (Fig. 3, Table
206 1).

207 For each step, equations 2 and 3 require knowledge of (1) an estimate of the initial $\delta^{56}$Fe
208 of the parent melt; (2) the crystallizing phase assemblage and proportion of phases; (3) the
209 amount (Fig. 3) and isotopic composition of Fe in each phase.

210 (1) The starting $\delta^{56}$Fe of the modeled liquid was fixed at 0.17‰ (Table 1). This value was
211 chosen to match the observed $\delta^{56}Fe_{WR}$ value at the base of the UUMZ (see Results below),
212 however, the initial $\delta^{56}Fe_{liquid}$ assumption has no bearing on the trends produced by the model.

213 (2) Normative abundances of each phase are based upon values reported by *VanTongeren*
214 *et al.* [2010] (Figs. 1, 2; Table 1), and all approximations of abundances from whole rock data
215 were verified within 2-3 modal% by point-counting of a representative thin section. Due to the
216 presence of large (meters to tens of meters) and small (cm) scale modal layering in the UUMZ,
217 the modal abundance of an individual hand-sample may not be representative of the liquidus
218 proportions. To account for this in our modeling of the liquid line of descent, we fit a line
219 through all of the normative abundances from *VanTongeren et al.* (2010) with stratigraphic
220 height (Fig. 2). In the UUMZ, pyroxene modal abundance generally decreases with increasing
221 stratigraphic height (from 50% at the base to 15% at the roof); above cumulus magnetite
222 saturation, oxide modal abundance generally increases (from 2% to 15%); and above olivine
223 saturation, its normative abundance remains relatively constant, at approximately 15% (although
224 it varies between 0 and 35%; Fig. 2). Based on this observation, the "projected" abundance
225 calculated from the best-fit line at each stratigraphic height, and therefore each % liquid
226 remaining step, was used in our liquid line of descent modeling (Table 1, "Step 1" of the
227 working model in Supporting Material).

228 The abundance of an individual mineral ($X_{mineral}$) was considered to be 0 until the
229 stratigraphic height at which it appears as a cumulus phase (pyroxene: 2200 m and 100% liquid
230 remaining; magnetite: ~2850 m and ~80% liquid remaining; olivine: ~3500 m and ~55% liquid
231 remaining).

232 (3) The FeO content of each phase was also incorporated in order to accurately portray
233 the effect of each phase on the whole rock isotopic composition by compensating for mineral
234 phases that are abundant (Fig. 2) but do not contain much Fe (e.g., plagioclase) (Fig. 3, details
235 below).

236 The Fe isotope composition of each mineral phase was calculated or assigned based upon
237 published data. All fractionation factors ($\Delta^{56}Fe_{phaseA\text{-}phaseB}$) used in the model are from previously
238 published field- or lab-based studies and are calculated by incorporating T and converting to
239 $\Delta^{56}Fe_{phaseA\text{-}phaseB}$ by the relationship: $\Delta^{57}Fe_{phaseA\text{-}phaseB} / 1.5 = \Delta^{56}Fe_{phaseA\text{-}phaseB}$. The use of these
240 fractionation factors also requires an assumption of equilibrium. The temperature-dependent
241 equations for each cumulus Fe-bearing mineral are:

242 $\Delta^{56}Fe_{pyroxene\text{-}melt} \leq -0.25 * (10^6/T^2) / 1.5$ [*Sossi et al.,* 2012]

243 $\Delta^{56}Fe_{magnetite\text{-}melt} = 0.2 * (10^6/T^2) / 1.5$ [*Sossi et al.,* 2012]

244 $\Delta^{56}Fe_{magnetite\text{-}fayalite} = 0.30 * (10^6/T^2) / 1.5$ [*Shahar et al.,* 2008]

245 The $\Delta^{56}Fe_{pyroxene\text{-}melt}$ and $\Delta^{56}Fe_{magnetite\text{-}melt}$ equations are derived from measurements of
246 samples from the Red Hill Intrusion, described in section 1, which is a sill containing dolerite
247 and granophyre that was injected in a single event and evolved as a closed system [*Sossi et al*.,
248 2012, section 1]. $\Delta^{56}Fe_{fayalite\text{-}magnetite}$ is based on data obtained from a series of experiments over a
249 range in temperatures performed by *Shahar et al.* [2008] and is consistent with the study of
250 *Roskosz et al.* [2015]. The experimental approach utilized the three-isotope method in which a

"spike" of one isotope of Fe is added to one experimental phase and time-series runs are performed. In this way, equilibrium can be graphically projected if not fully obtained. These equations are the only mineral-melt fractionation factors available in the literature, to our knowledge, which are applicable for the T range and composition of the UUMZ. Clinopyroxene and orthopyroxene compostiions were calculated by using the same fractionation factor since Fe isotope fractionation is not expected to differ [*Roskosz et al.*, 2015], while ilmenite was treated like fayalite, consistent with the findings of *Sossi et al.* 2017. Magnetite and olivine were not included in the model until the height at which they appear as a cumulus phase (Figs. 1, 2, Table 1), even though small amounts of intercumulus magnetite and olivine occur in the rocks of the UUMZ below these levels.

Due to the temperature dependence of isotope fractionation, we calculate crystallization temperatures by utilizing results from the $T_{REE}$ thermometer of *Sun et al.* [2013] and *Liang et al.* [2013], who observe a linear change in temperature from ~1250°C at 2200 m to ~1050°C at 3500 m in the UUMZ. Above ~3500 m in the stratigraphy, the REE thermometer is no longer calibrated for the compositional range. However, due to the linearity of the thermometer below 3500 m, we are able to calculate the temperatures for the stratigraphy from 3500 m to 4625 m by assuming the same slope in temperature vs. stratigraphic height. Over the course of the entire UUMZ stratigraphy, the crystallization temperature in our model decreases by ~15°C per 5% decrease in percent liquid remaining (i.e., at each model step). Using the two-pyroxene thermometer or the QUILF program would be insufficient here since both approaches would only allow for the determination of closure temperature of the system. Since layered intrusions are generally expected to cool slowly, those temperatures would likely be reset considerably.

Lastly, since the whole rocks contain a normative abundance of plagioclase of up to 86% (Fig. 2), it was incorporated into the model despite this phase's low Fe content. Little work has been done thus far to constrain the Fe isotopic composition of plagioclase in terrestrial magmatic systems, but *Wang* [2013] found that lunar regolith plagioclase has a $\delta^{56}Fe$ of 0.15-0.30‰. Thus, we fixed the $\delta^{56}Fe_{plagioclase}$ value at 0.20‰. However, it is important to note that plagioclase contributes such a small amount of FeO to the system that despite its abundance, it does not significantly influence the model regardless of its Fe isotopic value.

For a working version of the model with annotations that reiterate the justification of parameters described here, please consult the Supplementary File.

## 2.2 Model Results

The results of our fractional crystallization model for the UUMZ are shown in Fig. 3. Our model reveals three important trends: (1) despite the positive mineral-melt fractionation factor for magnetite ($\Delta^{56}Fe_{mgt\text{-}melt} =\sim 0.2 * 10^6/T^2 / 1.5$; *Sossi et al.,* 2012), the low abundance of magnetite relative to pyroxene and olivine in the UUMZ samples buffers the effect of magnetite crystallization on the evolution of $\delta^{56}Fe$ in the liquid. Consequently, our model predicts only a subtle change in the $\delta^{56}Fe$ of the liquid from 0.17‰ to 0‰ through the whole UUMZ and no major shift in slope after magnetite or olivine saturation (Fig. 4). (2) The model predicts an overall decrease in the $\delta^{56}Fe_{WR}$ of about 0.11‰. This is likely due to the decreasing proportion of FeO contributed to the whole rock by magnetite relative to the isotopically lighter phases pyroxene and olivine in the cumulus assemblage (Fig. 3). The amount of FeO in the whole rock that is contributed by pyroxene and olivine increases with stratigraphic height while the proportion of FeO in the whole rock from magnetite remains constant. (3) The model also

296 predicts no significant change in $\delta^{56}Fe_{mgt}$ with stratigraphic height, varying just 0.08‰
297 throughout the UUMZ (Table 1, Supplementary Material).

298 The lack of change in $\delta^{56}Fe$ predicted by the fractional crystallization model is somewhat
299 surprising given previously published fractionation factors for single minerals [e.g., *Schuessler et*
300 *al.*, 2007; *Shahar et al.,* 2008; *Sossi et al.* 2012], which predict a large crystal-liquid
301 fractionation. In order to test our model results, we present data on $\delta^{56}Fe$ for whole rock and
302 magnetite mineral separates in the UUMZ of the Bushveld Complex.
303

304 **3 Sampling and Analytical Methods**

305 3.1 Sampling Details

306 Samples were collected from exposed sections of the eastern limb of the RLS and are the
307 same as those analyzed in the studies of *VanTongeren et al.* [2010], *VanTongeren and Mathez*
308 [2012], and *VanTongeren and Mathez* [2013] (Fig. 1). We analyzed 22 whole rock samples,
309 measuring the Fe isotopic composition of the UUMZ approximately every 100 m within the ~2.5
310 km thick section (Fig. 1). Above cumulus magnetite saturation, magnetite is the dominant
311 control on the Fe concentration in the whole rock in that it contributes more FeO than any other
312 Fe-bearing phase (Fig. 3). Accordingly, magnetite separates were analyzed from each sample
313 where available (20 of 22 samples) in order to determine their control on the Fe isotopic
314 composition of the whole rocks.
315

316 3.2 Sample Preparation

317 To prepare the samples for isotopic analysis, magnetite was first separated by hand
318 magnet and subsequently picked under a binocular microscope at 30x magnification. Only

magnetite grains without visible impurities were used. About 5-10 mg of whole rock samples was measured out so that no more than ~500 μg of Fe was processed through the columns later. Magnetite samples were measured out to weigh 0.5 to 1 mg. Crushed whole rock samples were first digested in a solution of HF and $HNO_3$ on a hot plate and dried down. Magnetite and whole rock samples were digested on a hotplate in *aqua regia*, dried down, and digested and dried again in 8N HCl prior to column chemistry. The 1 ml columns were filled with Biorad AG1-X8 ion exchange resin, which was conditioned prior to samples being loaded. First, the column reservoir was filled with 8M $HNO_3$, followed by 1 full reservoir of $H_2O$, 1 full reservoir of 0.1N HCl, and finally 2ml 8N HCl. The sample was dissolved again on the hotplate in 0.2 ml 8N HCl for loading. Next, the resin was rinsed four times by using 0.5 ml of 8N HCl. Then, to elute the Fe 0.5 ml of 8N $HNO_3$ was introduced, and then 1 ml of 0.5N HCl was introduced twice. Next, 0.5 ml of $H_2O$, 1 ml 8N $HNO_3$, and then 0.5 ml of $H_2O$ were used in succession to elute the rest of the Fe. *Zambardi et al.* [2014] used the same column chromatography method and demonstrated that Ca, Na, Al, and Mg were eluted prior to Fe and did not linger in the columns. They also checked that Fe was not being eluted early with the matrix and routinely checked that the column yields were ~99%. Zinc may also be of concern when using this elution scheme for digested whole rock samples, however, *Millet et al.* [2012] demonstrated that Zn only interferes with Fe during analysis by multi-collector inductively coupled plasma mass spectrometer (MC-ICP-MS) when the two elements are present in the same concentration. In these Bushveld samples, Zn concentrations vary between 50-180 ppm while Fe concentrations are never below 5 wt%.

Samples were then dried down and re-dissolved in 20 μl of concentrated $HNO_3$ before being dried down one last time before analysis. All acids used were sub-boiling distilled and all

water used was ultrapure. During each session of column chromatography, we produced 1 blank sample to monitor for potential environmental contamination. The Fe blank was insignificant (<0.1%) relative to the amount of Fe loaded on the column.

### 3.3 Analytical Details

After performing the column chromatography, samples were dissolved in 2% $HNO_3$ for introduction to the mass spectrometer. Stable Fe isotope analyses were performed on whole rock ($\delta^{56}Fe_{WR}$) and magnetite ($\delta^{56}Fe_{mgt}$) samples by using a Nu Plasma HR MC-ICP-MS at the University of Illinois, Urbana-Champaign. Mass resolution was >6000 and samples were run in dry plasma mode with a desolvating nebulizer system. All standard and sample solutions were run at concentrations of ~1ppm. We employed the $^{57}Fe$-$^{58}Fe$ double-spike method of *Millet et al*. [2012] by adding 0.5ppm of well-characterized spike solution containing a known composition of $^{57}Fe$ and $^{58}Fe$ to all measured samples and standards, including those used to bracket sample measurements. The double spike deconvolution was performed online during the analytical method, wherein the precise isotopic composition of the double spike solution was taken into account. It entails an online iteration that subtracts from the measured values the contributions from the double spike solution and calculates mass bias with convergence within ten calculation cycles. The IRMM-014 (Institute of Reference Materials and Measurements standard number 014) bracketing standard was run between every sample analysis and secondary standards (BCR-2, UI-Fe) were run as every fourth sample. This standard-sample bracketing method is widely used to correct for instrumental mass bias and improve data precision. To correct for interferences with Ni on $^{58}Fe$ and Cr on $^{54}Fe$, each sample and standard analysis included measurements of these two elements, and the data were used to adjust the analyzed Fe values

365 accordingly. The average ratio (±2σ) of 52/54 was 0.0001 (±0.002) and the average ratio of
366 60/58 was 0.00006 (±0.0001).
367
368 **4 Results**
369 Data are reported in Table 2 and Figure 5 in the conventional delta notation, following
370 the equation:
371 $$\delta^{56}Fe_{sample}\ (‰) = [(^{56}Fe/^{54}Fe)_{sample} / (^{56}Fe/^{54}Fe)_{IRMM\text{-}014} - 1] * 1000 \quad \text{(eqn. 4)}$$
372 Each unknown sample and standard measurement included 2-3 repeated analyses. USGS rock
373 powder standard BCR-2 was also processed alongside unknown samples. BCR-2 and in-house
374 standard UI-Fe were analyzed throughout each session to monitor accuracy and instrumental
375 drift. The precision reported is given based on the 2SD of 2-3 repeat analyses, and reported as
376 0.03‰ if there was no variation between the analyses (i.e., 2σ=0.00‰). USGS rock powder
377 standard BCR-2 gives 0.06 ±0.09‰ (average over one five-day analytical session; n=9), which is
378 within error of other studies [*Dauphas et al.,* 2009; *Wombacher et al.,* 2009; *Craddock and*
379 *Dauphas*, 2011; *Huang et al.,* 2011; *Sossi et al.,* 2012]. The in-house standard UI-Fe gives $\delta^{56}Fe$
380 = 0.71‰ ±0.04‰ (2SD, n=8 throughout the same five-day session).
381 We observe little variability within a tight range of $\delta^{56}Fe_{WR}$ values throughout the
382 UUMZ; $\delta^{56}Fe_{WR}$ (±2σ) ranges from -0.01 ±0.03‰ to 0.21 ±0.09‰ ($\delta^{56}Fe_{WR}$ average ~0.10
383 ±0.09‰, excluding isotopically light outlier B06-062, $\delta^{56}Fe_{WR}$ = -0.15 ±0.07‰). There is no
384 correlation with stratigraphic height and therefore magma evolution within the UUMZ (Fig. 5,
385 Table 2). Measured $\delta^{56}Fe_{mgt}$ (±2σ) are consistently isotopically heavier than their whole rock
386 counterparts, an expected pattern based on experimental data [*Shahar et al.,* 2008] and
387 measurements of natural samples [e.g., *Heimann et al.,* 2008]. In general, however, the

388 stratigraphic variations in UUMZ magnetite are also unsystematic ($\delta^{56}Fe_{mgt}$ = 0.28 ±0.05‰ to
389 0.86 ±0.07‰; average = 0.48 ±0.16‰) (Fig. 5).
390
391 **5 Discussion**
392 5.1 The Effect of Fractional Crystallization on Fe Isotope Evolution
393 The observed absence of significant variation or a systematic trend in the Fe isotope
394 composition of the UUMZ whole rock samples is consistent with our model (Fig. 6), based upon
395 calculated parameters rather than measured ones. Our simple model mimics the overall variation
396 observed in the measured Fe isotope composition of the UUMZ, particularly between ~80 and
397 30% liquid remaining, and therefore demonstrates that fractional crystallization plays an
398 important role in the Fe isotope evolution of the UUMZ. Because the calculations of the
399 predicted $\delta^{56}Fe_{WR}$ values are principally controlled by the abundance of individual Fe-bearing
400 phases, each of which prefers a certain isotope, oxidation state of Fe, or coordination, the whole
401 rock Fe isotope composition appears to be buffered by the changing Fe-bearing mineral
402 assemblage. This agrees with previous work, such as *Sossi et al.* [2012]. As we observe in the
403 measured values, we predict a tight range and unsystematic variability in the overall trend
404 throughout the stratigraphy (Fig. 6).
405 In the uppermost portion of the stratigraphy (above 30% liquid remaining, ~4000 m
406 above the Merensky Reef), the modeled and measured whole rock values diverge more, with the
407 measured $\delta^{56}Fe$ values behaving quite erratically. This may be due to the fact that processes
408 other than fractional crystallization play a key role in the formation of these rocks.
409 5.1.1 Comparison of modeled and measured $\delta^{56}Fe$

410 The simplified fractional crystallization model for Fe isotopes (section 2) predicts that
411 values for $\delta^{56}$Fe in the whole rock and liquid would not change significantly with stratigraphic
412 height in the UUMZ using the observed normative abundances of mineral phases. Modeled
413 whole rock values are consistently lighter than measured whole rock in the UUMZ, with the
414 exception of one sample prior to magnetite crystallization. Although we did not expect for our
415 model to identically match the measured values, the differences between the predicted Fe isotope
416 values and measured whole rock data may be a result of several factors.
417 First, the presence of an unknown amount of trapped melt in the whole rock samples
418 could result in values higher or lower than model, depending on the relative proportions of
419 cumulus pyroxene and magnetite in the whole rock. If the melt is indeed isotopically heavier
420 than the whole rock as our model predicts, this could explain why our measured $\delta^{56}$Fe values are
421 more positive than the modeled ones. While there is currently no observed evidence of trapped
422 melt in the samples analyzed, perhaps the Fe isotope data provides an indication.
423 We should also consider the model calculations themselves, which can provide insight
424 into the measured values. Importantly, the fractionation factors were calculated from previously
425 published experimental and natural samples, which may have crystallized under conditions
426 different from those of the UUMZ. They also require an assumption of equilibrium. While there
427 are published beta factors for some of the phases (which agree with the magnetite fractionation
428 factor in our model; *Roskosz et al.*[2015]), the paucity of these data at relevant conditions for
429 every considered phase (ol, opx, cpx, mgt, ilm, melt*, and* plag) hindered the attempt to use these
430 more recent data in the model. This may also be the case for the set isotopic value of plagioclase,
431 however the value does not significantly influence the model.

Another important aspect to note is that our modeled liquid, upon which our modeled whole rock relies, is based on *trends* in normative abundances with increasing stratigraphic height. This was done to compensate for the layered nature of the intrusion today. On the other hand, the calculated whole rock is based upon the normative abundances themselves. This projection of modes used in the calculation of the liquid may cause some smoothing of the modeled results that are not reflected in the measured data.

Processes that occurred during or after the cooling of the intrusion may also have influenced the measured values. For example, diffusion of Fe at sub-solidus conditions could alter the $\delta^{56}$Fe values of individual minerals, and in the case of oxides this effect may be unequal [*Dziony et al*., 2014]. *Chen et al.* [2014] proposed this hypothesis to explain the discrepancy in the $\delta^{56}$Fe values measured in magnetite and ilmenite collected from the Baima layered intrusion, China, where olivine and pyroxene were apparently unaltered by re-equilibration of Fe isotopes. Therefore, our magnetite samples might be isotopically heavier than they were during crystallization, and this may also explain the erratic nature of the data (Figs. 5, 6). However, it is important to note that sub-solidus re-equilibration may occur to affect the $\delta^{56}$Fe of individual phases but mobility of Fe is low, meaning that the whole rock faithfully records its magmatic signature. A major conclusion from previous Fe isotope studies is that whole rock compositions show systematic changes with index of differentiation and are thus best suited to understanding differentiation processes [*Poitrasson*, 2006].

Notably, the top portion (>4000m above the MR, <35% liquid remaining) of the analyzed stratigraphy displays scattered measured values not mirrored by our estimations (Fig. 6). *VanTongeren and Mathez* [2012] proposed that the uppermost 625 m of the Upper Zone underwent large-scale silicate liquid immiscibility, and the study of *Fischer et al.* [2016]

455 identified the presence of both Fe-rich and Si-rich melt inclusions trapped in apatite grains within
456 the Upper Zone. Our data within the potential liquid immiscibility portion do follow markedly
457 different trends than the data below it (Fig. 5). There currently exists no published fractionation
458 factor to describe Fe isotope behavior between Fe-rich and Si-rich immiscible melts, but
459 previous work does predict a measurable fractionation of Fe isotopes between the two melts.
460 *Zhu et al.* [2015] performed calculations based on thermal diffusion that predict an
461 enrichment of isotopically heavy Fe in the Si-rich melt relative to the bulk Fe-melt from which it
462 formed. This is consistent with the work of *Dauphas et al.* [2014], although their conclusion is
463 based upon a different mechanism; they observe an increase in the force constants of Fe bonds in
464 silicate glasses with $SiO_2$ content accompanying enrichment in isotopically heavy Fe. However,
465 the fractionation of Fe isotopes between two such melts is quite complex and may also be
466 controlled by factors including the growth rate of the immiscible melt, the concentration of $SiO_2$
467 and Fe in each melt, and Fe diffusivity. It is also likely that there is an unknown degree of
468 isotopic re-equilibrium between the two melts, which would attenuate the relative differences in
469 $\delta^{56}Fe$ caused by liquid immiscibility. We cannot tell at this time whether the more Si-rich
470 samples above 4000m are isotopically heavier with respect to Fe isotopes due to liquid
471 immiscibility or the fact that they are more evolved.
472
473 5.2 Measured $\delta^{56}Fe_{mgt}$ and Potential Implications for the Formation of the UUMZ
474 Magnetitite Layers
475 One of the most well-known aspects of the Upper Zone of the Bushveld Complex is the
476 presence of over twenty layers of nearly mono-mineralic magnetite [*Molyneux*, 1974] (Fig. S2).
477 Proposed hypotheses for the origin of these layers include gravitational settling [e.g., *Cawthorn*

478 *and Ashwal,* 2009], periodic changes in $fO_2$ [e.g., *Klemm et al.,* 1982; *Reynolds et al.,* 1985]
479 possibly due to new pulses of magma added to the resident magma chamber [e.g., *Irvine and*
480 *Sharpe*, 1986], pressure fluctuations [*Cawthorn and McCarthy*, 1980], and silicate liquid
481 immiscibility [e.g., *Scoon and Mitchell*, 1994; *Harney and von Gruenewaldt*, 1995]. There is no
482 recorded change in $fO_2$ in the UUMZ rocks analyzed here [c.f. *VanTongeren and Mathez*, 2012],
483 and there is no change in the geochemical characteristics (isotopes, major and trace elements)
484 above and below magnetite layers [c.f. *Cawthorn and Ashwal,* 2009] that would indicate
485 formation due to new pulses of magma. Evidence for large-scale silicate liquid immiscibility
486 exists in the diorites at the top of the UUMZ [*VanTongeren and Mathez*, 2012]; however there is
487 no such evidence available from the lower portions of the UUMZ, which also contain abundant
488 magnetite layers.

489 Our measured $\delta^{56}Fe_{mgt}$ values are significantly but inconsistently isotopically heavier
490 than the measured $\delta^{56}Fe_{WR}$ values. Comparably high $\delta^{56}Fe_{mgt}$ have also been reported in the
491 Skaergaard [*Dziony et al.,* 2014]. Above and below the magnetitite layers, the measured Fe
492 isotope composition of the magnetite separates and corresponding whole rock samples do not
493 markedly change. The lack of change in $\delta^{56}Fe_{mgt}$ and $\delta^{56}Fe_{WR}$ above and below magnetite layers
494 in the UUMZ (Fig. S2) suggests that the formation of these horizons is likely due to
495 gravitational settling of magnetite as a result of normal fractional crystallization, consistent with
496 the conclusions of *Cawthorn and Ashwal* [2009]. However, with the information currently
497 available, further speculation about the formation of these layers is not possible.
498
499 5.3 Comparison of the Fe Isotope Systematics of the Bushveld with other Single-Event
500 Igneous Systems with Evidence of Fractional Crystallization

501 $\delta^{56}$Fe values of whole rock samples from the UUMZ are consistent with previous studies
502 of mafic or low silica intrusive igneous rocks (Fig. 7). *Sossi et al.* [2012] measured the $\delta^{56}$Fe
503 composition of 16 whole rock and 6 magnetite-pyroxene pairs from the ~420 m thick Red Hill
504 sill, Tasmania. This single injection of tholeiitic magma underwent fractional crystallization in a
505 closed system, similar to the UUMZ albeit on a significantly smaller scale. They report
506 increasing $\delta^{56}Fe_{WR}$ with decreasing whole rock MgO wt% until magnetite saturation (Fig. 7B),
507 and attributed this to the effects of fractional crystallization of Fe-bearing phases on the $Fe^{3+}/\Sigma Fe$
508 of the melt. *Teng et al.* [2008] report a similar range in MgO wt% versus Fe isotope composition
509 of whole rocks from Kilauea Iki, Hawaii, in that $\delta^{56}$Fe increases with decreasing MgO. *Sossi et*
510 *al.* suggested that systems open to $O_2$ (i.e., buffered at a specific $fO_2$) would not record
511 significant changes in $\delta^{56}Fe_{WR}$ until late in their crystallization history (i.e., higher $SiO_2$),
512 whereas those closed to $O_2$ (e.g., Red Hill, Kilauea Iki) should display increasing $\delta^{56}Fe_{WR}$
513 throughout the stratigraphy (Fig. 7B). Aside from differences in scale and layering, fayalite
514 disappears as a cumulus phase after magnetite saturation in the Red Hill sill while fayalite co-
515 crystallizes with magnetite throughout much of the top ~2 km of the Bushveld. Throughout the
516 UUMZ, magnetite-ilmenite pairs record equilibrium $fO_2$ values near FMQ-1 [e.g., *VanTongeren*
517 *and Mathez*, 2012], which is likely buffered by the presence of both fayalite and magnetite.
518 Thus, the lack of systematic changes in $fO_2$ and $\delta^{56}Fe_{WR}$ in the UUMZ is consistent with the
519 hypothesis of *Sossi et al.* [2012].
520
521 5.4. Comparison to the Baima Mafic Layered Intrusion
522 In the most comprehensive study of Fe isotope fractionation in layered mafic intrusions
523 to date, *Chen et al.* [2014] provide $\delta^{56}$Fe data for whole rock, olivine, pyroxene, magnetite,

ilmenite mineral separates throughout the stratigraphy of the Baima Intrusion, China. They observed little change in $\delta^{56}Fe_{WR}$ with increasing stratigraphic height, but they noticed a distinctive trend of increasing magnetite $\delta^{56}Fe$ values with height. To a first order, the increase in magnetite $\delta^{56}Fe$ appears to be the opposite of that observed in our study (the $\delta^{56}Fe_{mgt}$ composition of samples near magnetite saturation is higher than the $\delta^{56}Fe_{mgt}$ composition of samples in the uppermost portion of the UUMZ). However two important points must be considered: (1) The Baima Intrusion is unique in that the Basal and Lower Zones are dominated by Fe-Ti oxides, constituting up to 55 modal % of the rocks. The abundance of Fe-Ti oxides, and the ratio of magnetite/ilmenite, *decreases* with increasing stratigraphic height, which is opposite to what is observed in the UUMZ; (2) the Baima Intrusion received multiple pulses of magma throughout its crystallization history, and may not be a reliable record of closed system processes.

### 5.5 The Potential Effect of Ilmenite

Comparison with the Baima Intrusion also highlights the potential effect of sub-solidus re-equilibration between magnetite and co-existing Fe-bearing minerals (in particular ilmenite), which may contribute to the observed differences between the Baima and the UUMZ as well as the scatter in the measured $\delta^{56}Fe$ values at the top of the stratigraphy (Fig. 5, 6). *Chen et al.* [2014] observed that the extent to which magnetite and ilmenite exchange chemically depends upon their relative abundances within the rock. And in some cases, the magnetite likely retained its original $\delta^{56}Fe$ composition. On the other hand, the majority of the other Fe-bearing minerals that were analyzed (ol, cpx) had mantle-like Fe isotope compositions, interpreted to be largely unaffected by sub-solidus re-equilibration. *Dziony et al.* [2014] studied in detail Fe isotopic

differences between co-existing magnetite and ilmenite in a variety of settings, including variable lithology from seafloor drill core (IODP hole 1256D, East Pacific Rise), massive hydrothermal deposits from the Mid-Atlantic Ridge, and gabbros from the Skaergaard Intrusion Middle Zone. In addition to varying differences between the two oxides in each setting, *Dziony et al.* also observed variations in $\delta^{56}Fe_{mgt}$ within individual grains, which has been demonstrated in other studies as well. Although it is important to point out that many of their samples had experienced extensive sub-solidus fluid-rock interaction that likely modified the Fe isotope ratios, in general, magnetite was isotopically heavier than ilmenite. This is also consistent with the experimental work of *Sossi and O'Neill* [2017]. No correlation between the measured Fe isotope values of UUMZ whole rock and magnetite and the normative abundances of each of the oxides exists, however, we cannot rule out the accidental inclusion of a small amount of ilmenite in our magnetite fraction. Considering the information available for our UUMZ samples, disentangling the potential effect of ilmenite is not straightforward at this time.

## 6 Conclusions

We provide the first $\delta^{56}Fe$ data for whole rock and magnetite separates throughout the sequence of the UUMZ of the Bushveld Complex layered intrusion, the trends of which are consistent with a simple model based solely on fractional crystallization. Our model incorporates the normative abundances and FeO content of each Fe-bearing phase throughout the stratigraphy as well as published fractionation factors and calculated temperature changes. We predict no significant change in $\delta^{56}Fe$ in the whole rock or liquid during fractional crystallization of the multiply-saturated UUMZ. Measured $\delta^{56}Fe_{WR}$ values confirm this result, and do not change systematically with stratigraphic height, but do display slight variability that corresponds to

570 changes in pyroxene, magnetite, and olivine normative abundance. Our data demonstrate two
571 important points:

572 (1) While crystallization of a single mineral phase will have an effect on the Fe isotopic
573 evolution of the liquid, the overall effect of fractional crystallization of a multiply-saturated (i.e.,
574 buffered) nominally anhydrous Fe-rich tholeiitic magma will be minimal.

575 (2) The Fe isotopic composition of a multiply saturated magma is unlikely to change
576 significantly during fractional crystallization of magnetite if there is *competing* fractionation of
577 other Fe-bearing cumulus phases (in particular, olivine and pyroxene). Therefore, it is
578 fundamentally important to consider both the modal mineralogy and contribution of FeO by each
579 phase to the whole rock when interpreting whole rock Fe isotopic data of cumulate rocks.

580 **Acknowledgements and Data**

581 All data that support the conclusions of this paper can be found in the figures and tables
582 included here. Any data not produced by the authors are cited by the original published work. A
583 working, annotated example of the model is provided in the Supplementary Material. The
584 authors would like to thank Laura Sammon for her help in sample separation and Norbert Gajos
585 for his help during some of the analyses. Helpful reviews from Helen Williams, Franck
586 Poitrasson, Paolo Sossi, and 1 anonymous reviewer greatly improved the manuscript, as did the
587 editorial handling of Janne Blichert-Toft.

588 **References**

589 Cawthorn, R.G., and T.S. McCarthy, (1980), Variations in Cr content of magnetite from the
590 upper zone of the Bushveld complex – evidence for heterogeneity and convection
591 currents in magma chambers. Earth Planet. Sci. Lett., 46, 335-343, doi:10.1016/0012-
592 821X(80)90049-7.

593 Cawthorn, R.G., and L.D. Ashwal (2009), Origin of anorthosite and magnetitite layers in the
594 Bushveld Complex, constrained by major element compositions of plagioclase. J. Petrol.,
595 50, 1607-1637, doi:10.1093/petrology/egp042.
596 Charlier, B. and T. Grove (2012) Experiments on liquid immiscibility along tholeiitic liquid lines
597 of descent. Contrib. Mineral. Petrol., 164, 27-44, doi:10.1007/s00410-012-0723-y.
598 Chen, L-M., X-Y. Song, X-K. Zhu, X-Q. Zhang, S-Y. Yu, J-N. Yi, (2014), Iron isotope
599 fractionation during crystallization and sub-solidus re-equilibration: constraints from the
600 Baima mafic layered intrusion, SW China. Chem. Geol., 380, 97-109,
601 http://dx.doi.org/10.1016/j.chemgeo.2014.04.020.
602 Craddock, P.R., and N. Dauphas (2011), Iron isotopic compositions of geological reference
603 materials and chondrites. Geostand. Geoanal. Res., 35, 101-123,
604 doi:10.1016/j.epsl.2013.01.011.
605 Dauphas, N., P.R. Craddock, P.D. Asimow, V.C. Bennett, A.P. Nutman, D. Ohnenstetter, (2009),
606 Iron isotopes may reveal the redox conditions of mantle melting from Archean to present.
607 Earth Planet. Sci. Lett., 299, 255-267, doi:10.1016/j.epsl.2009.09.029.
608 Dauphas, N., M. Roskosz, E.E. Alp, D.R. Neuville, M.Y. Hu, C.K. Sio, F.L.H. Tissot, J. Zhao, L.
609 Tissandier, E. Médard, and C. Cordier (2014), Magma redox and structural controls on
610 iron isotope variations in Earth's mantle and crust. Earth Planet. Sci. Lett., 308, 127-140,
611 http://dx.doi.org/10.1016/j.epsl.2014.04.033.
612 Dziony, W., I. Horn, D. Lattard, J. Koepke, G. Steinhoefel, J.A. Schuessler, F. Holtz, (2014) In-
613 situ Fe isotope ratio determination in Fe-Ti oxides and sulfides from drilled gabbros and
614 basalt from the IODP Hole 1256D in the eastern equatorial Pacific. Chem. Geol., 363,
615 101-113, reserved, http://dx.doi.org/10.1016/j.chemgeo.2013.10.035.

616 Fischer L.A., M. Wang, B. Charlier, O. Namur, R.J. Roberts, I.V. Veksler, R.G. Cawthorn, F.
617 Holtz (2016) Immiscible iron- and silica-rich liquids in the Upper Zone of the Bushveld
618 Complex. Earth Planet. Sci. Lett., 443, 108-117.
619 Foden, J., P.A. Sossi, and C.M. Wawryk, (2015), Fe isotopes and the contrasting petrogenesis of
620 A-, I- and S-type granite. Lithos, 212-215, 32-44, doi:10.1016/j.lithos.2014.10.015.
621 Harney, D.M.W., and G. von Gruenewaldt (1995), Ore-forming processes in the upper part of
622 the Bushveld Complex, South Africa. J. African Earth Sci., 20, 77-89.
623 Heimann A., B.L. Beard, and C.M. Johnson (2008), The role of volatile exsolution and sub-
624 solidus fluid/rock interactions in producing high $^{56}Fe/^{54}Fe$ ratios in siliceous igneous
625 rocks. Geochim. Cosmochim. Acta, 72, 4379-4396, doi:10.1016/j.gca.2008.06.009.
626 Huang, F., P. Chakraborty, C.C. Lundstrom, C. Holmden, J.J.G. Glessner, S.W. Kieffer, and C.E.
627 Lesher (2010), Isotope fractionation in silicate melts by thermal diffusion. Nature, 464,
628 396-400, doi:10.1038/nature08840.
629 Irvine, T.N., and M.R. Sharpe (1986), Magma mixing and the origin of stratiform oxide ore
630 zones in the Bushveld and Stillwater Complexes, Metallogeny of Basic and Ultrabasic
631 Rocks, edited by M.J. Gallagher, et al., pp. 183-198, Institute of Mining Metallurgy,
632 London.
633 Klemm, D.D., R. Snethlage, R.M. Dehm, J. Henchel, R. Schmidt-Thomé (1982), The formation
634 of chromite and titanomagnetite deposits within the Bushveld Igneous Complex, Ore
635 Genesis: The State of the Art, Special Publication of the Society for Geology Applied to
636 Mineral Deposits, v.ol 2, edited by G.C. Amstutz, p. 351-370, Springer Berlin
637 Heidelberg, doi:10.1007/978-3-642-68344-2_35.
638 Kruger, F.J., R.G. Cawthorn, and K.L. Walsh (1987), Strontium isotopic evidence against

639 magma addition in the Upper Zone of the Bushveld Complex. Earth Planet. Sci. Lett., 84,
640 51-58, doi:10.1016/0012-821X(87)90175-0.
641 Liang, Y., C. Sun, L.D. Ashwal, and J.A. VanTongeren (2013), Spatial variations in temperature
642 across the Bushveld layered intrusion revealed by REE-in-plagioclase-pyroxene
643 thermometers with implications for magma chamber processes [abs.]: Transactions,
644 American Geophysical Union, abstract #V54B-07.
645 Liu, P-P., M-F. Zhou, B. Luais, D. Cividini, and C. Rollion-Bard (2014), Disequilibrium iron
646 isotopic fractionation during the high-temperature magmatic differentiation of the Baima
647 Fe-Ti oxide-bearing mafic intrusion, SW China. Earth Planet. Sci. Lett., 399, 21-29,
648 doi:10.1016/j.epsl.2014.05.0220012-821X.
649 Lundstrom, C.C. (2009), Hypothesis for the origin of convergent margin granitoids and Earth's
650 continental crust by thermal migration zone refining. Geochim. Cosmochim. Acta 73,
651 5709-5729, doi:10.1016/j.gca.2009.06.020.
652 Mathez, E. A., J.A. VanTongeren, and J. Schweitzer (2013), On the relationships between the
653 Bushveld Complex and its felsic roof rocks, part 1: petrogenesis of Rooiberg and related
654 felsites. Contrib. Mineral. Petrol., 166, 435-449, doi:10.1007/s00410-013-0884-3.
655 Millet, M., J. Baker, and C. Payne (2012), Ultra-precise stable Fe isotope measurements by high
656 resolution multi-collector inductively coupled plasma mass spectrometry with a $^{57}Fe$-$^{58}Fe$
657 double spike. Chem. Geol., 304-305, 18-25, doi:10.1016/j.chemgeo.2012.01.021.
658 Molyneux, T.G. (1974), A geological investigation of the Bushveld Complex in Sekhukhuneland
659 and part of the Steelpoort Valley. Trans. Geological Society of South Africa, 77, 329-
660 338.

661 Poitrasson, F., and R. Freydier (2005), Heavy iron isotope composition of granites determined by
662 high resolution MC-ICP-MS. Chem. Geol., 222, 132-147,
663 doi:10.1016/j.chemgeo.2005.07.005.
664 Poitrasson, F. (2006), On the iron isotope homogeneity level of the continental crust. Chem.
665 Geol., 235, 195-200, doi:10.1016/j.chemgeo.2006.06.010.
666 Polyakov, V.B. and S.D. Mineev (2000) The use of Mössbauer spectroscopy in stable isotope
667 geochemistry. Geochim. Cosmochim. Acta, 64, 849-865.
668 Polyakov, V.B., R.N. Clayton, J. Horita and S.D. Mineev (2007) Equilibrium iron isotope
669 fractionation factors of minerals: Reevaluation from the data of nuclear inelastic resonant
670 X-ray scattering and Mössbauer spectroscopy. Geochim. Cosmochim. Acta, 71, 3833-
671 3846, doi:10.1016/j.gca.2007.05.019.
672 Reynolds, I.M. (1985), The nature and origin of titaniferous magnetite-rich layers in the upper
673 zone of the Bushveld Complex; a review and synthesis. Econ. Geol., 80, 1089-1108.
674 Roskosz M., C.K.I. Cio, N. Dauphas, W. Bi, F.L.H. Tissot, M.Y. Hu, J. Zhao and E.E. Alp
675 (2015) Spinel-olivine-pyroxene equilibrium iron isotopic fractionation and applications to
676 natural peridotites. Geochim. Cosmochim. Acta, 169, 184-199,
677 http://dx.doi.org/10.1016/j.gca.2015.07.035.
678 Schuessler, J.A., R. Schoenberg, H. Behrens, and F. von Blanckenburg (2007), The experimental
679 calibration of the iron isotope fractionation factor between pyrrhotite and peralkaline
680 rhyoltic melt. Geochim. Cosmochim. Acta, 71, 417-433, doi:10.1016/j.gca.2006.09.012.
681 Schuessler, J.A., R. Schoenberg, and O. Sigmarsson (2009), Iron and lithium isotope systematics
682 of the Hekla volcano, Iceland—Evidence for Fe isotope fractionation during magma
683 differentiation. Chem. Geol., 258, 78-91, doi:10.1016/j.chemgeo.2008.06.021.

684 Schoenberg, R., M.A.W. Marks, J.A. Schuessler, F. von Blanckenburg, and G. Markl (2009), Fe
685 isotope systematics of coexisting amphibole and pyroxene in the alkaline igneous rock
686 suite of the Ilimaussaq Complex, South Greenland. Chem. Geol., 258, 65-77,
687 10.1016/j.chemgeo.2008.06.023.
688
689 Scoon, R.N., and A.A. Mitchell (1994), Discordant iron-rich ultramafic pegmatites in the
690 Bushveld Complex and their relationship to iron-rich intercumulus and residual liquids. J.
691 Petrol., 35, 881-917.
692 Shahar, A., E.D. Young, and C.E. Manning (2008), Equilibrium high-temperature Fe isotope
693 fractionation between fayalite and magnetite: An experimental calibration. Earth Planet.
694 Sci. Lett., 268, 330-338, doi:10.1016/j.epsl.2008.01.026.
695 Sossi, P.A., J.D. Foden, and G.P. Halverson (2012), Redox-controlled iron isotope fractionation
696 during magmatic differentiation: an example from the Red Hill intrusion, S. Tasmania.
697 Contrib. Mineral. Petrol., 164, 757-779, doi:10.1007/s00410-012-0769-x.
698 Sossi, P.A. and H. O'Neill (2017) The effect of bonding environment on iron isotope
699 fractionation between minerals at high temperature. Geochim. Cosmochim. Acta, 196,
700 121-143, http://dx.doi.org/10.1016/j.gca.2016.09.017.
701 Sun, C., Y. Liang, L. Ashwal, J. VanTongeren (2013), Temperature variations along
702 stratigraphic height across the Bushveld Complex with implications for magma chamber
703 processes in layered intrusions [abs]: Geological Society of America Abstracts with
704 Programs, 45, 390.

705 Tegner, C., R.G. Cawthorn and F.J. Kruger (2006) Cyclicity in the Main and Upper Zones of the
706 Bushveld Complex, South Africa: Crystallization from a Zoned Magma Sheet. J. Petrol.,
707 47, 2257-2279, doi:10.1093/petrology/egl043.
708 Telus, M., N. Dauphas, F. Moynier, F.L.H. Tissot, F-Z. Teng, P.I. Nabelek, P.R. Craddock, and
709 L.A. Groat (2012), Iron, zinc, magnesium and uranium isotopic fractionation during
710 continental crust differentiation: The tale from migmatites, granitoids, and pegmatites.
711 Geochim. Cosmochim. Acta,, 97, 247-265, http://dx.doi.org/10.1016/j.gca.2012.08.024.
712 Teng, F., N. Dauphas, and R.T. Helz (2008), Iron isotope fractionation during magmatic
713 differentiation in Kilauea Iki Lava Lake. Science, 320, 1620-1622,
714 doi:10.1126/science.1157166.
715 Teng, F., W.F. McDonough, R.L. Rudnick and R.J. Walker (2011) Diffusion-driven extreme
716 lithium isotopic fractionation in country rocks of the Tin Mountain pegmatite. Earth
717 Planet. Sci. Lett., 243, 701-710, doi:10.1016/j.epsl.2006.01.036.
718 VanTongeren, J.A., E.A. Mathez, and P.B. Kelemen (2010), A felsic end to Bushveld
719 differentiation. J. Petrol., 51, 1891-1942, doi:10.1093/petrology/egq042.
720 VanTongeren, J.A., and E.A. Mathez (2012), Large-scale liquid immiscibility at the top of the
721 Bushveld Complex. Geology, 40, 491-494, doi:10.1130/G32980.1.
722 VanTongeren, J.A., and E.A. Mathez (2013), Incoming magma composition and style of
723 recharge below the Pyroxenite Marker, Eastern Bushveld Complex, South Africa. J.
724 Petrol., 54, 1585-1605, doi:10.1093/petrology/egt024.
725 Wang, K. (2013), Iron isotope cosmochemistry, Ph.D dissertation, Dept. Earth and Planetary
726 Sciences, Washington University in St. Louis, St. Louis, Washington, USA.

727 Williams, H.M., A. H. Peslier, C. McCammon, A.N. Halliday, S. Levasseur, N. Teutsch, and J-P.
728 Burg (2005), Systematic iron isotope variations in mantle rocks and minerals: The effects
729 of partial melting and oxygen fugacity. Earth Planet. Sci. Lett., 235, 435-452,
730 doi:10.1016/j.epsl.2005.04.020.
731 Wombacher F., A. Eisenhauer, A. Heuser, and S. Weyer (2009). Separation of Mg, Ca and Fe
732 from geological reference materials for stable isotope ratio analyses by MC-ICP-MS and
733 double-spike TIMS. J. Anal. At. Spectrom, 24, 627-636, doi:10.1039/B820154D.
734 Young, E.D., C.E. Manning, E.A. Schauble, A. Shahar, C.A. Macris, C. Lazar, and M. Jordan
735 (2015), High-temperature equilibrium isotope fractionation of non-traditional stable
736 isotopes: Experiments, theory, and applications. Chem. Geol., 395, 176-195,
737 doi:10.1016/j.chemgeo.2014.12.0130009-2541.
738 Zambardi, T., C.C. Lundstrom, X. Li, M. McCurry (2014), Fe and Si isotope variations at Cedar
739 Butte volcano; insight into magmatic differentiation. Earth Planet. Sci. Lett., 405, 169-
740 179, doi:10.1016/j.epsl.2014.08.020.
741 Zhu D., B. Huiming, Y. Liu (2015), Non-traditional stable isotope behaviors in immiscible
742 silica-melts in a mafic magma chamber. Nature, Scientific Reports, doi:10.1038/srep175.

**Table 1.** Abbreviated compilation of model inputs. NA—modes were not available for that sample. For a working version of the model with accompanying justification of all terms reiterated from the text, please see the Supplementary Material.

| **% liquid remaining** | **100** | **95** | **90** | **85** | **80** | **75** | **70** | **65** | **60** | **55** | **50** | **45** | **40** | **35** | **30** | **25** | **20** | **15** |
|---|---|---|---|---|---|---|---|---|---|---|---|---|---|---|---|---|---|---|
| **Equivalent strat. height** | 2202.5 | 2345 | 2487.5 | 2630 | 2772.5 | 2915 | 3057.5 | 3200 | 3342.5 | 3485 | 3627.5 | 3770 | 3912.5 | 4055 | 4197.5 | 4340 | 4482.5 | 4625 |
| **Projected modes** | | | | | | | | | | | | | | | | | | |
| Plagioclase | 0.53 | 0.53 | 0.53 | 0.53 | 0.53 | 0.53 | 0.53 | 0.53 | 0.53 | 0.53 | 0.53 | 0.53 | 0.53 | 0.53 | 0.53 | 0.53 | 0.53 | 0.53 |
| Orthopyroxene | 0.312 | 0.278 | 0.244 | 0.210 | 0.176 | 0.143 | 0.109 | 0.075 | 0.041 | 0.007 | 0 | 0 | 0 | 0 | 0 | 0 | 0 | 0 |
| Clinopyroxene | 0.158 | 0.192 | 0.226 | 0.260 | 0.294 | 0.327 | 0.361 | 0.395 | 0.429 | 0.245 | 0.240 | 0.227 | 0.215 | 0.203 | 0.190 | 0.178 | 0.166 | 0.153 |
| Olivine | 0 | 0 | 0 | 0 | 0 | 0 | 0 | 0 | 0 | 0.15 | 0.15 | 0.15 | 0.15 | 0.15 | 0.15 | 0.15 | 0.15 | 0.15 |
| Magnetite | 0 | 0 | 0 | 0 | 0.004 | 0.012 | 0.021 | 0.029 | 0.037 | 0.045 | 0.054 | 0.062 | 0.070 | 0.078 | 0.087 | 0.095 | 0.103 | 0.111 |
| Ilmenite | 0 | 0 | 0 | 0 | 0.002 | 0.006 | 0.010 | 0.014 | 0.018 | 0.023 | 0.027 | 0.031 | 0.035 | 0.039 | 0.043 | 0.047 | 0.051 | 0.055 |
| **Fe content of each phase (FeO phase/FeO WR)** | | | | | | | | | | | | | | | | | | |
| Plagioclase | 0.067 | 0.057 | 0.049 | 0.042 | 0.037 | 0.032 | 0.028 | 0.024 | 0.021 | 0.019 | 0.016 | 0.014 | 0.012 | 0.010 | 0.009 | 0.007 | 0.006 | 0.005 |
| Orthopyroxene | 2.315 | 2.228 | 2.158 | 2.101 | 2.053 | 2.013 | 1.978 | 1.948 | 1.921 | 1.898 | 1.877 | 1.858 | 1.841 | 1.826 | 1.812 | 1.799 | 1.788 | 1.777 |
| Clinopyroxene | 0.526 | 0.604 | 0.666 | 0.718 | 0.761 | 0.797 | 0.828 | 0.855 | 0.879 | 0.900 | 0.919 | 0.936 | 0.951 | 0.964 | 0.977 | 0.988 | 0.999 | 1.008 |
| Olivine | 0 | 0 | 0 | 0 | 0 | 0 | 0 | 0 | 0 | 2.665 | 2.713 | 2.756 | 2.794 | 2.829 | 2.861 | 2.890 | 2.917 | 2.941 |
| Magnetite | 0 | 0 | 0 | 0 | 7.783 | 7.192 | 6.685 | 6.245 | 5.859 | 5.518 | 5.215 | 4.943 | 4.698 | 4.476 | 4.275 | 4.090 | 3.921 | 3.765 |
| Ilmenite | 0 | 0 | 0 | 0 | 4.501 | 4.160 | 3.866 | 3.612 | 3.388 | 3.191 | 3.016 | 2.859 | 2.717 | 2.589 | 2.472 | 2.365 | 2.268 | 2.178 |
| **δ56Fe of each phase (calculated)** | | | | | | | | | | | | | | | | | | |
| Liquid | 0.168 | 0.165 | 0.154 | 0.144 | 0.135 | 0.126 | 0.116 | 0.106 | 0.096 | 0.086 | 0.074 | 0.063 | 0.052 | 0.042 | 0.033 | 0.025 | 0.018 | 0.012 |
| Plagioclase | 0.2 | 0.2 | 0.2 | 0.2 | 0.2 | 0.2 | 0.2 | 0.2 | 0.2 | 0.2 | 0.2 | 0.2 | 0.2 | 0.2 | 0.2 | 0.2 | 0.2 | 0.2 |
| Orthopyroxene | 0.060 | 0.054 | 0.041 | 0.027 | 0.014 | 0.001 | -0.012 | -0.027 | -0.041 | -0.057 | -0.074 | -0.091 | -0.108 | -0.125 | -0.141 | -0.156 | -0.171 | -0.185 |
| Clinopyroxene | 0.060 | 0.054 | 0.041 | 0.027 | 0.014 | 0.001 | -0.012 | -0.027 | -0.041 | -0.057 | -0.074 | -0.091 | -0.108 | -0.125 | -0.141 | -0.156 | -0.171 | -0.185 |
| Olivine | 0.125 | 0.121 | 0.109 | 0.097 | 0.087 | 0.076 | 0.064 | 0.053 | 0.040 | 0.028 | 0.013 | -0.001 | -0.015 | -0.028 | -0.041 | -0.052 | -0.063 | -0.074 |
| Magnetite | 0.253 | 0.253 | 0.245 | 0.238 | 0.231 | 0.225 | 0.218 | 0.211 | 0.204 | 0.197 | 0.188 | 0.179 | 0.172 | 0.165 | 0.159 | 0.155 | 0.152 | 0.149 |
| Ilmenite | 0.125 | 0.121 | 0.109 | 0.097 | 0.087 | 0.076 | 0.065 | 0.053 | 0.042 | 0.030 | 0.016 | 0.003 | -0.010 | -0.022 | -0.034 | -0.044 | -0.054 | -0.062 |
| **Measured Data** | | | | | | | | | | | | | | | | | | |
| Sample name | B07-009 | B06-062 | B06-064 | B06-065 | B06-067 | | | B07-057 | B06-020* | B07-061 | B06-054 | B06-042 | B06-039 | B06-029 | B07-027 | B06-037 | B07-036 | B07-041 |
| Strat. height | 2210 | 2325 | 2495 | 2620 | 2775 | | | 3122 | 3260 | 3425 | 3634 | 3741 | 3925 | 4083 | 4232 | 4305 | 4460 | 4590 |
| % liquid equivalent | 99.74 | 95.70 | 89.74 | 85.35 | 79.91 | | | 67.74 | 62.89 | 57.11 | 49.77 | 46.02 | 39.56 | 34.02 | 28.79 | 26.23 | 20.79 | 16.23 |
| **Modes from LSQR Matlab (*VanTongeren et al.*, 2010)** | | | | | | | | | | | | | | | | | | |
| Plagioclase | 0.45 | 0.37 | 0.54 | 0.56 | 0.49 | NA | NA | 0.58 | 0.49 | 0.84 | 0.79 | 0.44 | 0.46 | 0.46 | 0.54 | 0.55 | 0.46 | 0.42 |
| Orthopyroxene | 0.31 | 0.49 | 0.21 | 0.22 | 0.23 | NA | NA | 0.14 | 0.19 | 0.06 | 0.00 | 0.00 | 0.00 | 0.00 | 0.00 | 0.00 | 0.00 | 0.00 |
| Clinopyroxene | 0.22 | 0.13 | 0.25 | 0.21 | 0.26 | NA | NA | 0.16 | 0.19 | 0.01 | 0.09 | 0.29 | 0.30 | 0.10 | 0.05 | 0.06 | 0.16 | 0.20 |
| Olivine | 0.00 | 0.00 | 0.00 | 0.00 | 0.00 | NA | NA | 0.00 | 0.00 | 0.00 | 0.05 | 0.17 | 0.12 | 0.24 | 0.23 | 0.22 | 0.24 | 0.19 |
| Magnetite | 0.00 | 0.00 | 0.00 | 0.00 | 0.00 | NA | NA | 0.08 | 0.09 | 0.04 | 0.04 | 0.03 | 0.06 | 0.07 | 0.07 | 0.07 | 0.00 | 0.02 |
| Ilmenite | 0.00 | 0.00 | 0.00 | 0.00 | 0.00 | NA | NA | 0.02 | 0.01 | 0.02 | 0.02 | 0.04 | 0.04 | 0.04 | 0.04 | 0.04 | 0.05 | 0.04 |
| **Modeled Whole Rock Fe Isotope Composition based on Observed Modes and Calculated Liquid Composition** | | | | | | | | | | | | | | | | | | |
| Whole Rock δ56Fe | 0.06 | 0.07 | 0.03 | 0.02 | 0.01 | NA | NA | 0.10 | 0.09 | 0.04 | 0.04 | 0.01 | 0.02 | 0.02 | 0.02 | 0.00 | -0.07 | -0.06 |

*This is the mode of B06-021.

748 **Table 2.** $\delta^{56}Fe$ values from whole rock and magnetite analyses with associated 2σ and lithology
749 of the accompanying unit.

| Stratigraphic position relative to the Merensky Reef (m) | Sample Number | Latitude (S)[2] | Longitude (E)[2] | Equivalent % liquid remaining | $\delta^{56}Fe_{WR}$(‰) | 2σ | $\delta^{56}Fe_{magnetite}$ (‰)[1] | 2σ[1] | Lithology |
|---|---|---|---|---|---|---|---|---|---|
| 2210 | B07-009 | 24°51.778' | 29°58.114' | 99.74 | 0.06 | 0.09 | 0.61 | 0.06 | gabbro |
| 2325 | B06-062 | 24°51.778' | 30°01.770' | 95.70 | -0.15 | 0.07 | NA | NA | gabbro |
| 2495 | B06-064 | 24°51.851' | 30°01.842' | 89.74 | 0.06 | 0.04 | 0.69 | 0.08 | gabbro |
| 2620 | B06-065 | 24°51.858' | 30°01.565' | 85.35 | 0.19 | 0.13 | 0.65 | 0.08 | gabbro |
| 2775 | B06-067 | 24°51.917' | 30°01.398' | 79.91 | 0.09 | 0.07 | 0.47 | 0.11 | gabbro |
| 3122 | B07-057 | 24°48.985' | 29°58.275' | 67.74 | 0.15 | 0.08 | 0.86 | 0.07 | gabbro |
| 3260 | B06-020 | 24°48.974' | 29°58.149' | 62.89 | 0.12 | 0.07 | 0.34 | 0.03 | gabbro |
| 3425 | B07-061 | 24°48.914' | 29°57.798' | 57.11 | 0.16 | 0.07 | NA | NA | anorthosite |
| 3515 | B06-024 | 24°48.910' | 29°57.711' | 53.95 | 0.08 | 0.08 | 0.28 | 0.05 | troctolite |
| 3634 | B06-054 | 24° 48.763' | 29°57.186' | 49.77 | 0.07 | 0.08 | 0.53 | 0.06 | gabbro |
| 3741 | B06-042 | 24°48.776' | 29°57.036' | 46.02 | 0.08 | 0.05 | 0.61 | 0.04 | gabbro |
| 3925 | B06-039 | 24°48.857' | 29°56.833' | 39.56 | -0.01 | 0.03 | 0.59 | 0.04 | gabbro |
| 4083 | B06-029 | 24°48.895' | 29°56.650' | 34.02 | 0.08 | 0.05 | 0.37 | 0.07 | troctolite |
| 4232 | B07-027 | 24°49.072' | 29°56.433' | 28.79 | 0.21 | 0.09 | 0.35 | 0.09 | diorite |
| 4305 | B06-037 | 24°48.747' | 29°56.407' | 26.23 | 0.09 | 0.02 | 0.30 | 0.05 | diorite |
| 4355 | B06-055 | 24°51.874' | 29°54.756' | 24.47 | 0.12 | 0.06 | 0.38 | 0.02 | diorite |
| 4460 | B07-036 | 24°51.845' | 29°54.607' | 20.79 | 0.07 | 0.03 | 0.32 | 0.03 | diorite |
| 4508 | B07-037 | 24°51.827' | 29°54.550' | 19.11 | 0.16 | 0.05 | 0.63 | 0.17 | diorite |
| 4530 | B07-038 | 24°51.823' | 29°54.519' | 18.33 | 0.02 | 0.06 | 0.38 | 0.02 | diorite |
| 4555 | B07-039 | 24°51.800' | 29°54.488' | 17.46 | 0.18 | 0.04 | 0.63 | 0.05 | diorite |
| 4573 | B07-040 | 24°51.794' | 29°54.465' | 16.82 | 0.06 | 0.06 | 0.38 | 0.05 | diorite |
| 4590 | B07-041 | 24°51.829' | 29°54.430' | 16.23 | 0.07 | 0.03 | 0.56 | 0.03 | diorite |

[1]NA indicates that not enough pure magnetite could be separated from the sample for Fe isotope analysis.
[2]GPS coordinates form VanTongeren et al. (2010), VanTongeren and Mathez (2012) and VanTongeren and Mathez (2013).

750
751

752 Figure Captions

753 **Figure 1.** a) geologic map of the Bushveld Complex and sampling sites for this study; b)
754 observed modal mineralogy throughout the UUMZ; c) the change in whole rock Mg# with
755 stratigraphic height throughout the UUMZ (all data from VanTongeren et al., 2010). In panel a,
756 all shades of blue in correspond to zones within the Rustenburg Layered Suite (teal = Upper
757 Zone, blue = Main Zone; navy blue = Lower Zone; dark blue = Critical Zone). Purple =
758 Dullstroom Formation; Green = Damwal Formation; Yellow = Kwaggasnek Formation; Red =
759 Schrikkloof Formation. Yellow dots and larger circles denote sampling locations within the map.
760
761 **Figure 2.** Normative abundances of constituent minerals with stratigraphic height. Lines indicate
762 the trend of "projected modal abundances" used in the fractional crystallization model (See
763 Supplementary Material for details). Due to the lack of trend in the normative abundance of
764 clinopyroxene with stratigraphic height, the projected normative abundance of clinopyroxene
765 was calculated as Cpx [modal%] = 1 – Plag [modal%] – Opx [modal%] – Oxide [modal%] – Ol
766 [modal%].
767
768 **Figure 3.** Observed FeO (wt%) of whole rock and mineral phases with stratigraphic height.
769 Lines indicate the compositional trend used in the fractional crystallization model.
770
771 **Figure 4**. Predicted evolution of the Fe isotope composition of the liquid and whole rock (WR)
772 based only on the projected and observed normative abundances, respectively (see "Step 1" for
773 the liquid and "Step 2" for the whole rock in the Supplementary Material). The model
774 incorporates published fractionation factors (pyroxene, magnetite, olivine), available published
775 $\delta^{56}Fe_{plagioclase}$ data, calculated crystallization temperatures over the stratigraphy, and the Fe

776 content of each phase. The % liquid remaining is calculated for each stratigraphic height
777 assuming 15% magma loss from the UUMZ to form some portion of the Rooiberg Group lavas
778 and/or Rashoop Granophyres (e.g., *VanTongeren et al.,* 2010; *Mathez et al.,* 2013). Approximate
779 saturation levels for magnetite and fayalite are noted with solid black lines at about 80% and
780 55% liquid remaining, respectively.
781
782 **Figure 5.** Measured Fe isotope compositions of whole rock (circles) and magnetite (diamonds)
783 samples plotted at stratigraphic height relative to the Merensky Reef. These data are compared to
784 the normative abundances of phases from the base of the UUMZ (Pyroxenite Marker at 2200 m)
785 to the roof (4625 m). All normative abundance approximations from whole rock data were
786 verified within 2-3 modal% by point-counting of a representative thin section and observed
787 modal % values were calculated by least squares by incorporating measured geochemical data
788 (modified from *VanTongeren et al.*, 2010). Error bars are 2σ. Ap—apatite saturation; ol—olivine
789 saturation; mgt—magnetite saturation.
790
791 **Figure 6.** Comparison of the modeled evolution of the Fe isotope composition of the whole rock
792 (WR) predicted solely from fractional crystallization (see "Step 2" in the Supplementary
793 Material) and the measured WR values (error bars are 2σ).
794
795 **Figure 7.** Whole rock Bushveld Complex $\delta^{56}$Fe values (black circles, error bars are 2σ) from this
796 study plotted versus (a) whole rock $SiO_2$ content and (b) MgO content with other published
797 studies on igneous whole rocks that evolved from a single event closed to $O_2$ gain/loss. The
798 isotopic range is consistent between the studies, and additional scatter within the Bushveld data

799 is likely due to its layered nature. White squares – Kilauea Iki, Hawaii, USA (*Teng et al.,* 2008);
800 gray triangles – Red Hill Intrusion, Tasmania (*Sossi et al.,* 2012). *Only *Teng et al.* samples with
801 MgO content >7wt.% were plotted, since these data are thought to reflect fractional
802 crystallization processes.

**Figure 1.**

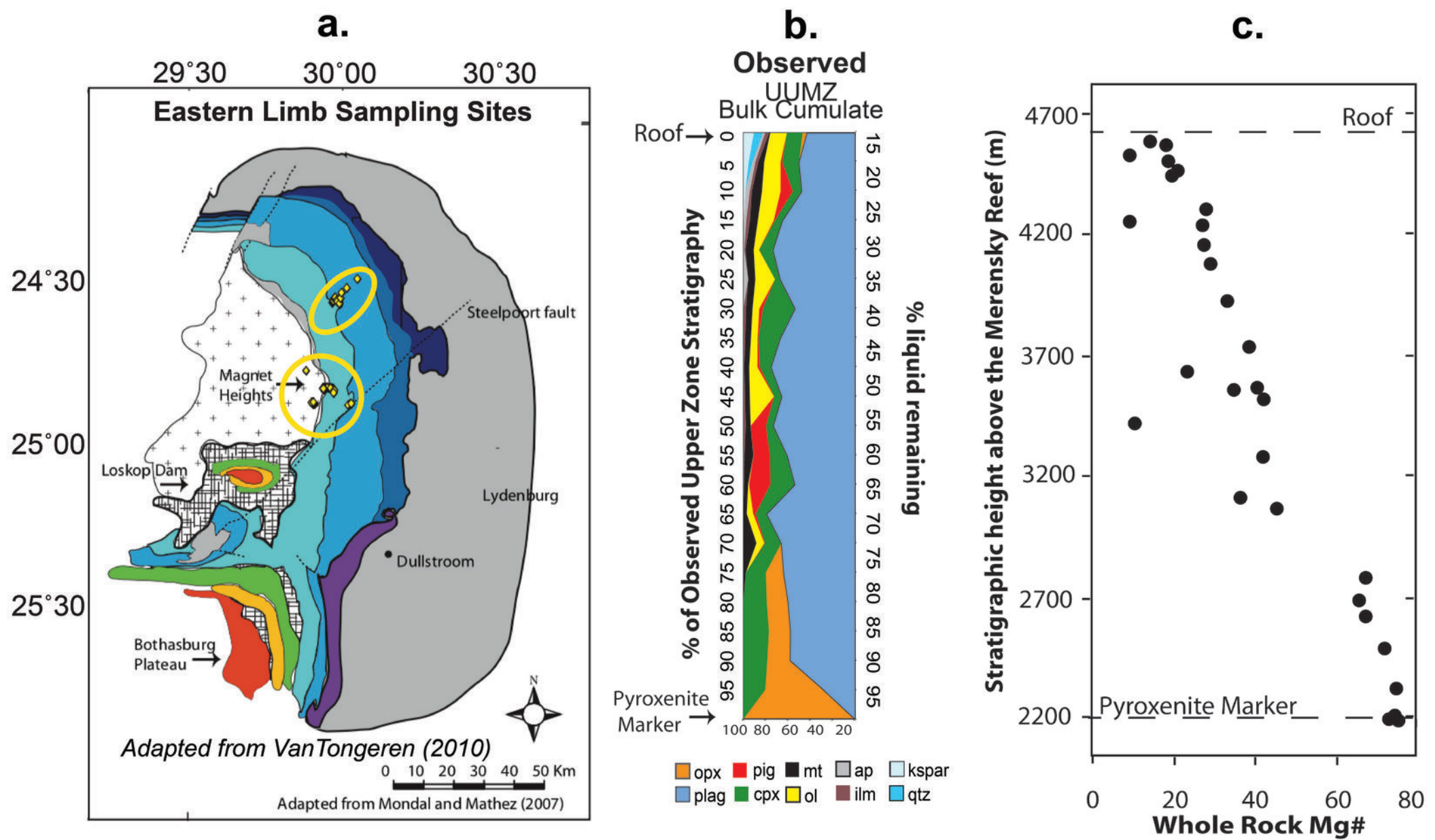
a.
29°30
30°00
30°30
Eastern Limb Sampling Sites
24°30
25°00
25°30
Steelpoort fault
Magnet Heights
Loskop Dam
Lydenburg
Dullstroom
Bothasburg Plateau
N
Adapted from VanTongeren (2010)
0 10 20 30 40 50 Km
Adapted from Mondal and Mathez (2007)
b.
Observed
UUMZ
Bulk Cumulate
Roof
Pyroxenite Marker
% of Observed Upper Zone Stratigraphy
% liquid remaining
0 5 10 15 20 25 30 35 40 45 50 55 60 65 70 75 80 85 90 95
15 20 25 30 35 40 45 50 55 60 65 70 75 80 85 90 95
100 80 60 40 20
opx
pig
mt
ap
kspar
plag
cpx
ol
ilm
qtz
c.
Stratigraphic height above the Merensky Reef (m)
4700
4200
3700
3200
2700
2200
Roof
Pyroxenite Marker
0 20 40 60 80
Whole Rock Mg#

**Figure 2.**

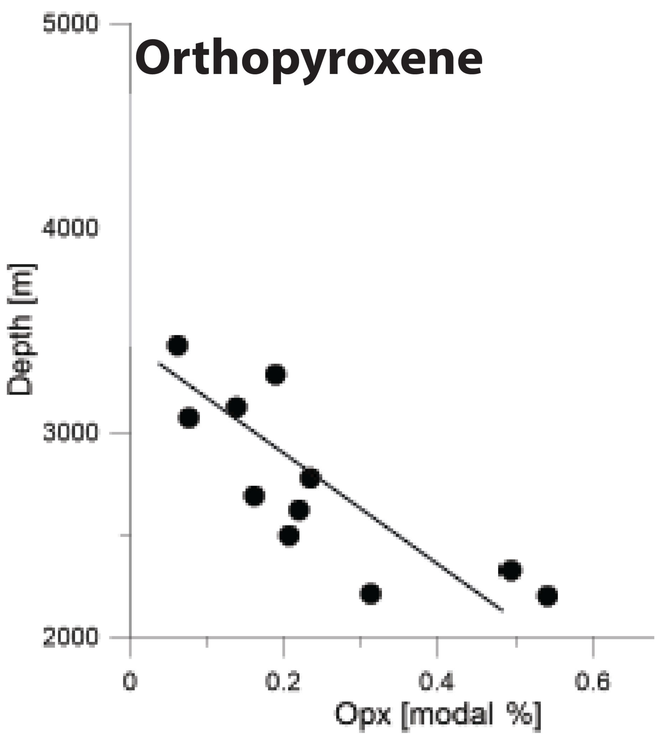
Orthopyroxene
Depth [m]
5000
4000
3000
2000
0
0.2
0.4
0.6
Opx [modal %]

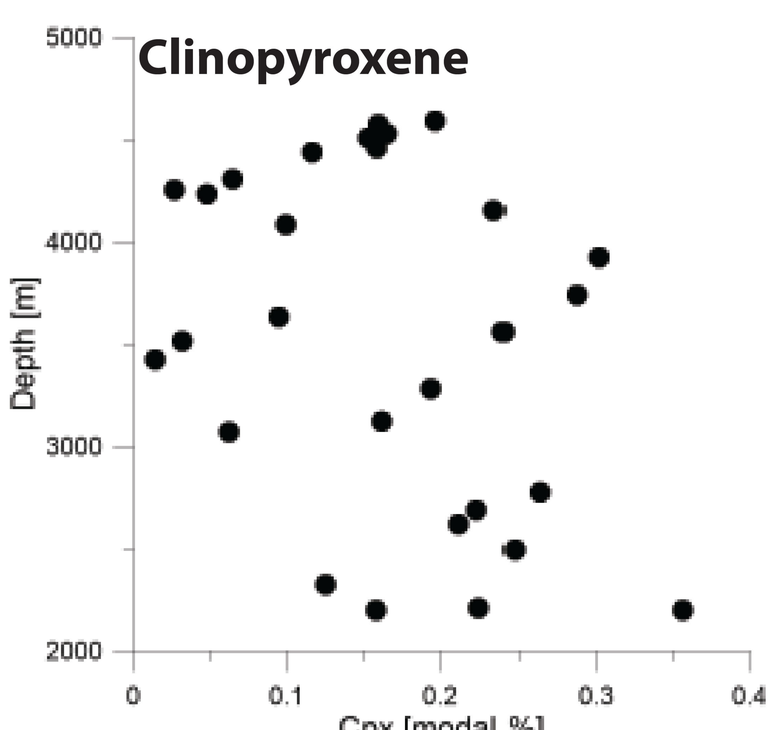
Clinopyroxene
Depth [m]
5000
4000
3000
2000
0
0.1
0.2
0.3
0.4
Cpx [modal %]

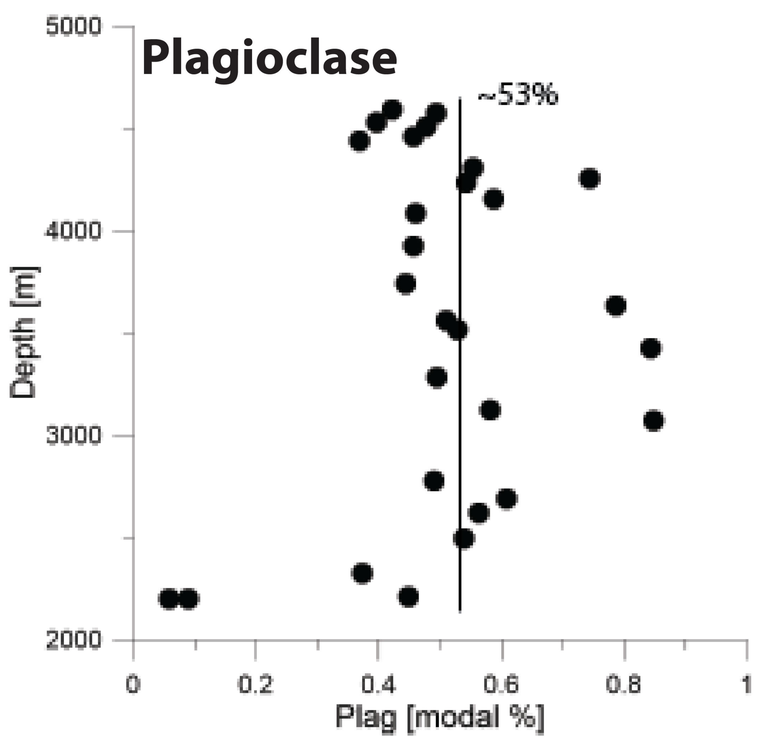
Plagioclase
~53%
Depth [m]
5000
4000
3000
2000
0
0.2
0.4
0.6
0.8
1
Plag [modal %]

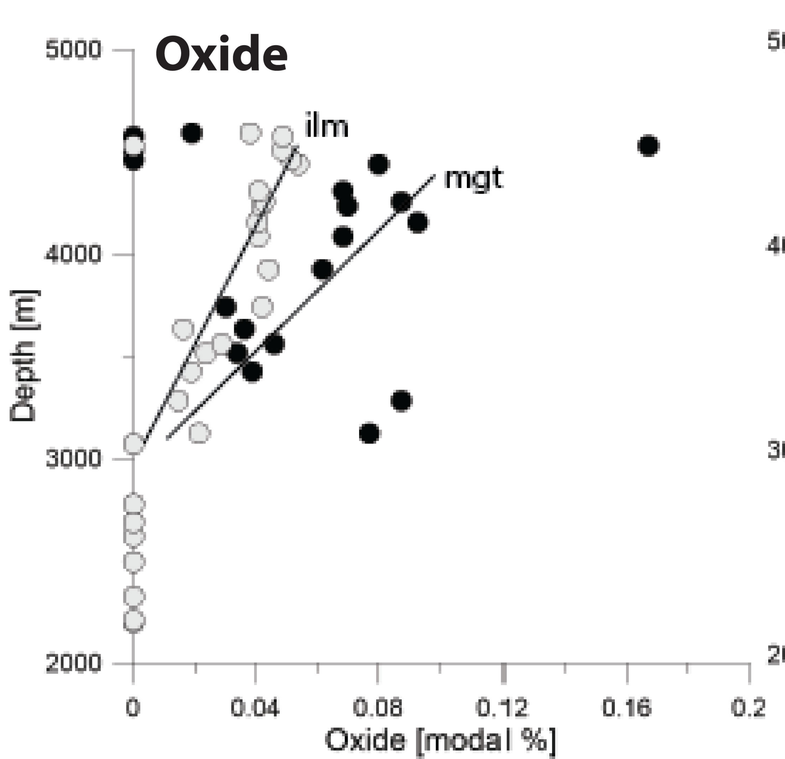
Oxide
ilm
mgt
Depth [m]
5000
4000
3000
2000
0
0.04
0.08
0.12
0.16
0.2
Oxide [modal %]

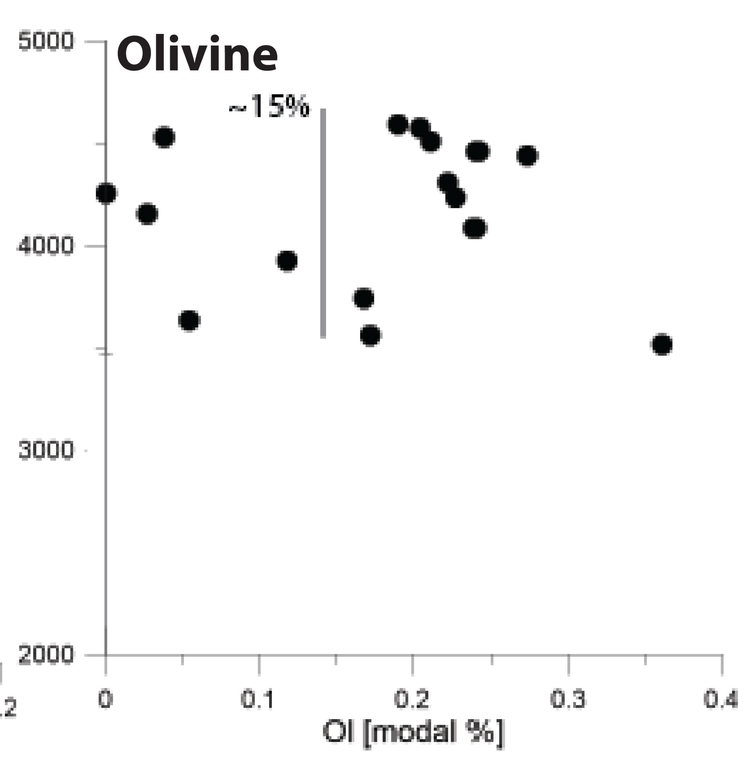
Olivine
~15%
5000
4000
3000
2000
0
0.1
0.2
0.3
0.4
Ol [modal %]

**Figure 3.**

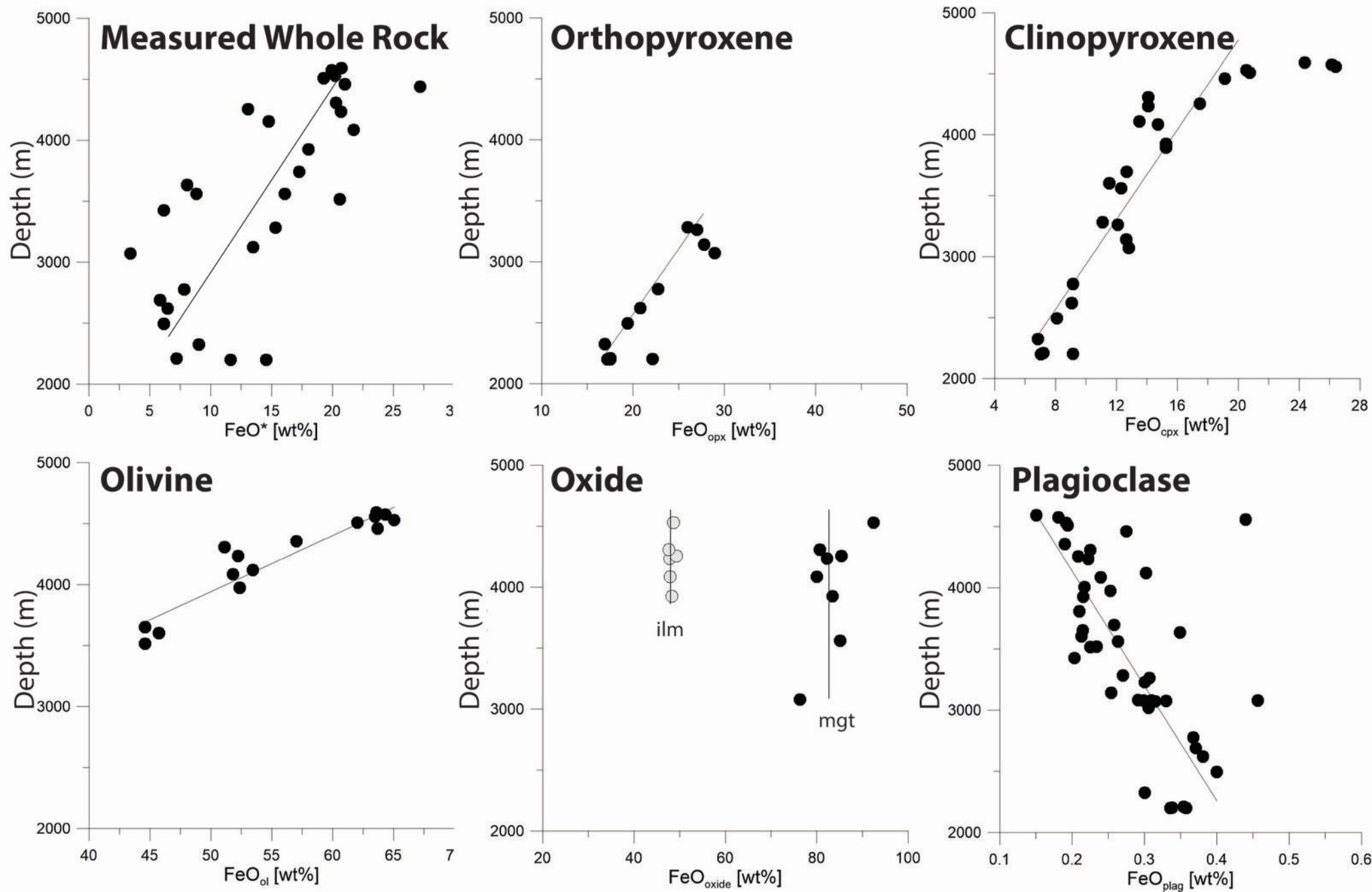
Measured Whole Rock
Depth (m)
FeO* [wt%]
Orthopyroxene
FeO$_{opx}$ [wt%]
Clinopyroxene
FeO$_{cpx}$ [wt%]
Olivine
FeO$_{ol}$ [wt%]
Oxide
ilm
mgt
FeO$_{oxide}$ [wt%]
Plagioclase
FeO$_{plag}$ [wt%]

**Figure 4.**

# Predicted $\delta^{56}$Fe evolution of liquid and whole rock throughout UUMZ

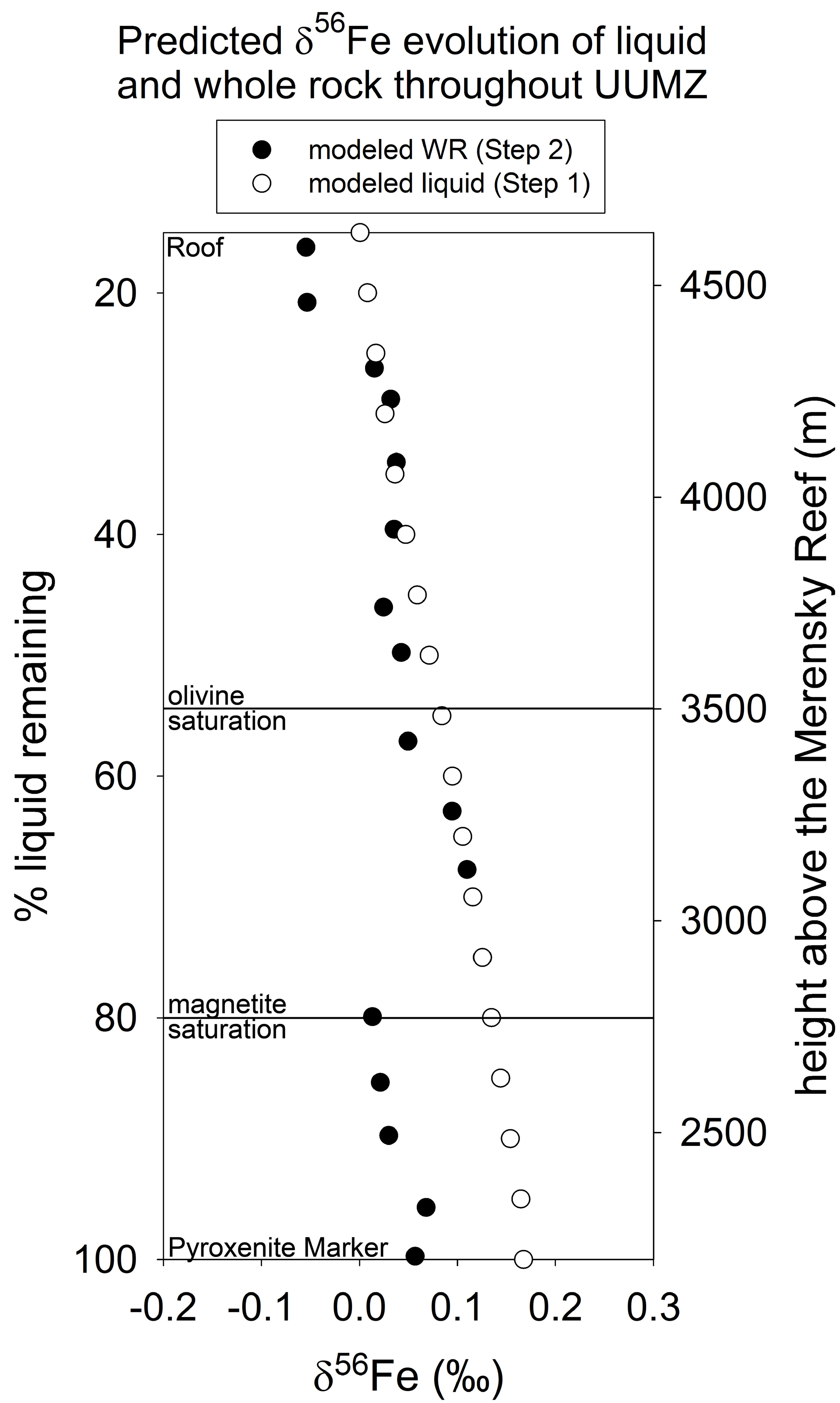

**Figure 5.**

$\delta^{56}Fe_{WR}$
$\delta^{56}Fe_{mgt}$
opx
plag
pig
cpx
mgt
ol
ap
ilm
kspar
qtz
Roof
4500
4000
3500
3000
2500
ap
ol
mgt
stratigraphic height (m) relative to Merensky Reef
% liquid remaining
15 20 25 30 35 40 45 50 55 60 65 70 75 80 85 90 95
-0.2 0.0 0.2 0.4 0.6 0.8 1.0
$\delta^{56}$Fe (‰)
100 80 60 40 20
observed modal %
Pyroxenite Marker

**Figure 6.**

# Modeled and measured $\delta^{56}$Fe evolution of whole rock throughout the UUMZ

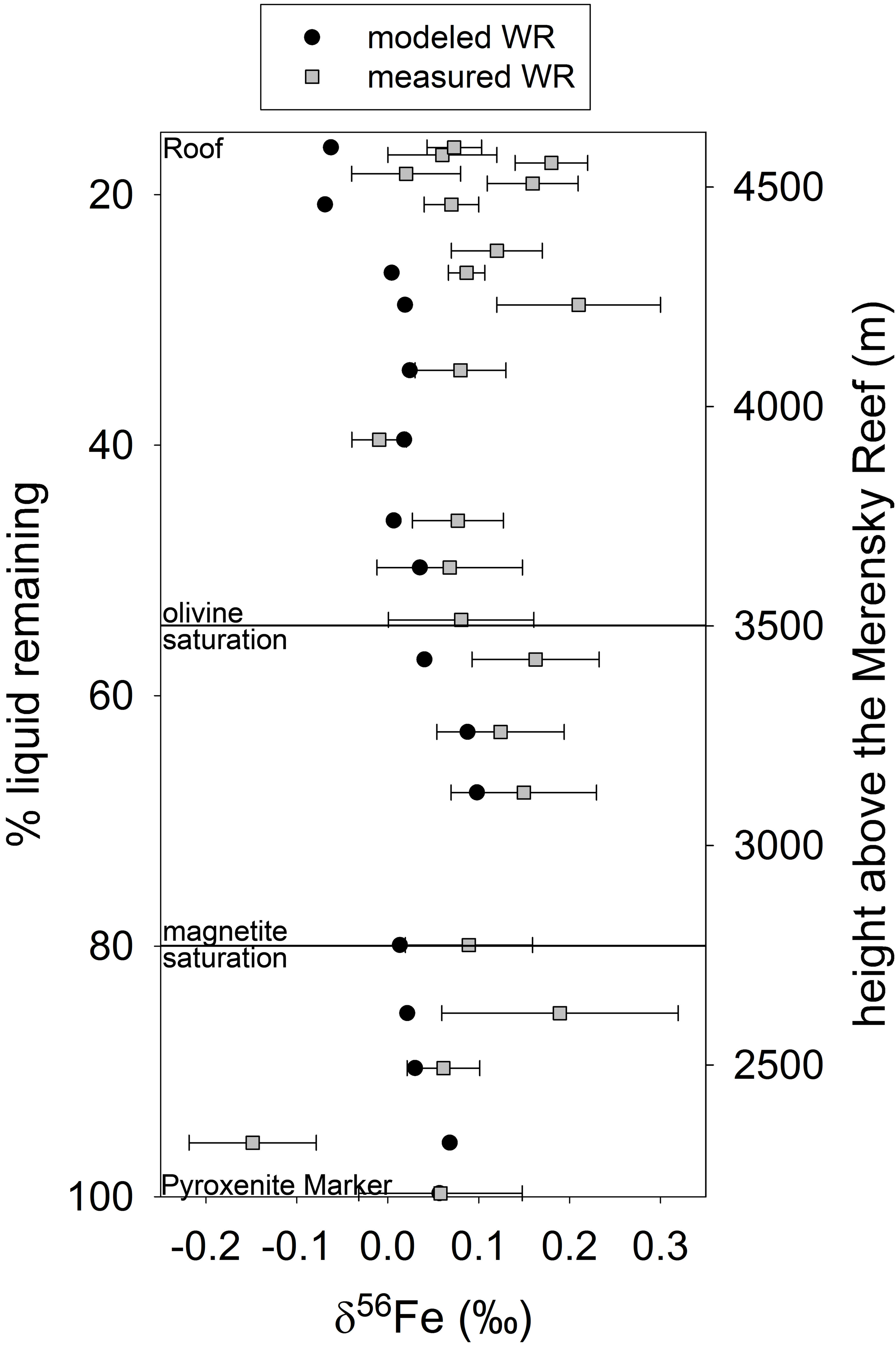

**Figure 7.**

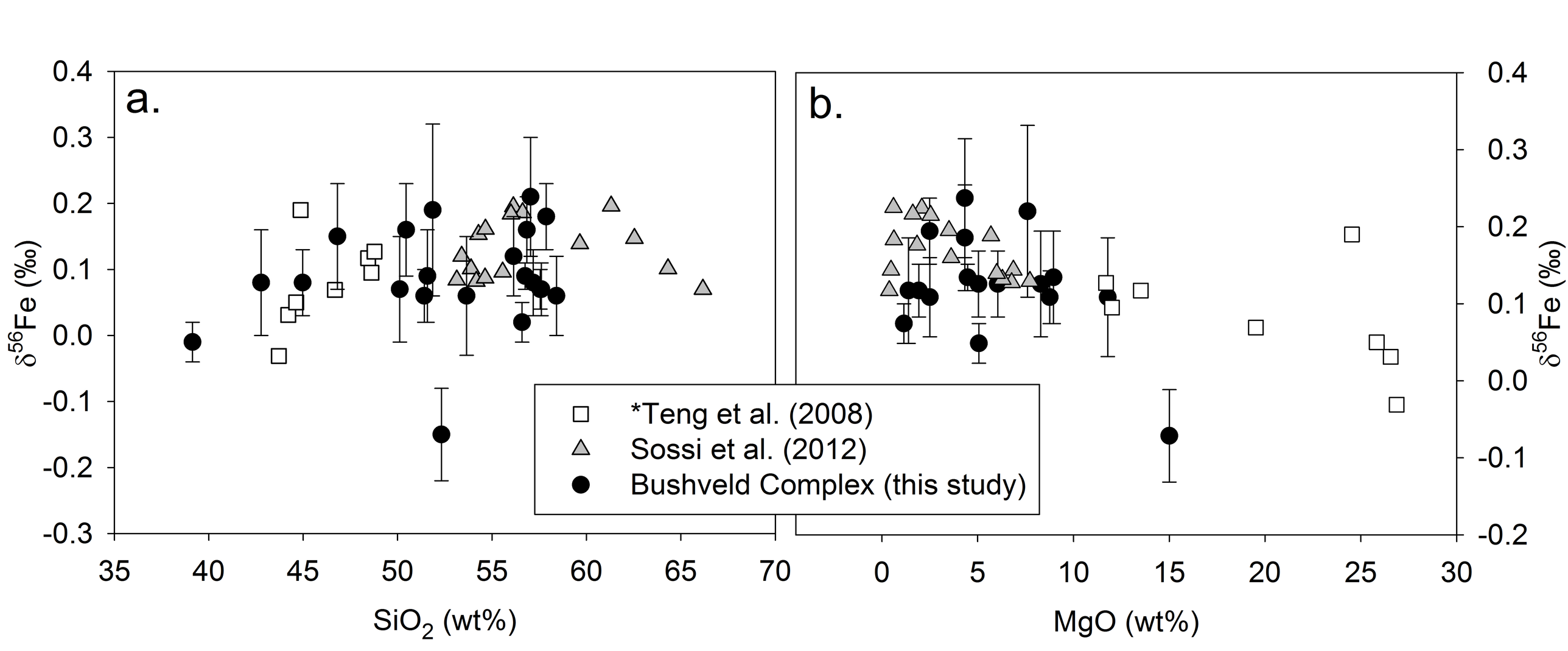
a.
b.
0.4
0.3
0.2
0.1
0.0
-0.1
-0.2
-0.3
δ56Fe (‰)
35
40
45
50
55
60
65
70
SiO2 (wt%)
0
5
10
15
20
25
30
MgO (wt%)
*Teng et al. (2008)
Sossi et al. (2012)
Bushveld Complex (this study)

**Table 1.** Abbreviated compiliation of model inputs. NA—modes were not available for that sample. For a working version of the model with accompanying justification of all terms reiterated from the text, please see the Supplementary Material.

| **% liquid remaining** | **100** | **95** | **90** | **85** | **80** | **75** | **70** | **65** | **60** | **55** | **50** | **45** | **40** | **35** | **30** | **25** | **20** | **15** |
|---|---|---|---|---|---|---|---|---|---|---|---|---|---|---|---|---|---|---|
| **Equivalent strat. height** | 2202.5 | 2345 | 2487.5 | 2630 | 2772.5 | 2915 | 3057.5 | 3200 | 3342.5 | 3485 | 3627.5 | 3770 | 3912.5 | 4055 | 4197.5 | 4340 | 4482.5 | 4625 |
| **Projected modes** | | | | | | | | | | | | | | | | | | |
| Plagioclase | 0.53 | 0.53 | 0.53 | 0.53 | 0.53 | 0.53 | 0.53 | 0.53 | 0.53 | 0.53 | 0.53 | 0.53 | 0.53 | 0.53 | 0.53 | 0.53 | 0.53 | 0.53 |
| Orthopyroxene | 0.312 | 0.278 | 0.244 | 0.210 | 0.176 | 0.143 | 0.109 | 0.075 | 0.041 | 0.007 | 0 | 0 | 0 | 0 | 0 | 0 | 0 | 0 |
| Clinopyroxene | 0.158 | 0.192 | 0.226 | 0.260 | 0.294 | 0.327 | 0.361 | 0.395 | 0.429 | 0.245 | 0.240 | 0.227 | 0.215 | 0.203 | 0.190 | 0.178 | 0.166 | 0.153 |
| Olivine | 0 | 0 | 0 | 0 | 0 | 0 | 0 | 0 | 0 | 0.15 | 0.15 | 0.15 | 0.15 | 0.15 | 0.15 | 0.15 | 0.15 | 0.15 |
| Magnetite | 0 | 0 | 0 | 0 | 0.004 | 0.012 | 0.021 | 0.029 | 0.037 | 0.045 | 0.054 | 0.062 | 0.070 | 0.078 | 0.087 | 0.095 | 0.103 | 0.111 |
| Ilmenite | 0 | 0 | 0 | 0 | 0.002 | 0.006 | 0.010 | 0.014 | 0.018 | 0.023 | 0.027 | 0.031 | 0.035 | 0.039 | 0.043 | 0.047 | 0.051 | 0.055 |
| **Fe content of each phase (FeO phase/FeO WR)** | | | | | | | | | | | | | | | | | | |
| Plagioclase | 0.067 | 0.057 | 0.049 | 0.042 | 0.037 | 0.032 | 0.028 | 0.024 | 0.021 | 0.019 | 0.016 | 0.014 | 0.012 | 0.010 | 0.009 | 0.007 | 0.006 | 0.005 |
| Orthopyroxene | 2.315 | 2.228 | 2.158 | 2.101 | 2.053 | 2.013 | 1.978 | 1.948 | 1.921 | 1.898 | 1.877 | 1.858 | 1.841 | 1.826 | 1.812 | 1.799 | 1.788 | 1.777 |
| Clinopyroxene | 0.526 | 0.604 | 0.666 | 0.718 | 0.761 | 0.797 | 0.828 | 0.855 | 0.879 | 0.900 | 0.919 | 0.936 | 0.951 | 0.964 | 0.977 | 0.988 | 0.999 | 1.008 |
| Olivine | 0 | 0 | 0 | 0 | 0 | 0 | 0 | 0 | 0 | 2.665 | 2.713 | 2.756 | 2.794 | 2.829 | 2.861 | 2.890 | 2.917 | 2.941 |
| Magnetite | 0 | 0 | 0 | 0 | 7.783 | 7.192 | 6.685 | 6.245 | 5.859 | 5.518 | 5.215 | 4.943 | 4.698 | 4.476 | 4.275 | 4.090 | 3.921 | 3.765 |
| Ilmenite | 0 | 0 | 0 | 0 | 4.501 | 4.160 | 3.866 | 3.612 | 3.388 | 3.191 | 3.016 | 2.859 | 2.717 | 2.589 | 2.472 | 2.365 | 2.268 | 2.178 |
| **δ56Fe of each phase (calculated)** | | | | | | | | | | | | | | | | | | |
| Liquid | 0.168 | 0.165 | 0.154 | 0.144 | 0.135 | 0.126 | 0.116 | 0.106 | 0.096 | 0.086 | 0.074 | 0.063 | 0.052 | 0.042 | 0.033 | 0.025 | 0.018 | 0.012 |
| Plagioclase | 0.2 | 0.2 | 0.2 | 0.2 | 0.2 | 0.2 | 0.2 | 0.2 | 0.2 | 0.2 | 0.2 | 0.2 | 0.2 | 0.2 | 0.2 | 0.2 | 0.2 | 0.2 |
| Orthopyroxene | 0.060 | 0.054 | 0.041 | 0.027 | 0.014 | 0.001 | -0.012 | -0.027 | -0.041 | -0.057 | -0.074 | -0.091 | -0.108 | -0.125 | -0.141 | -0.156 | -0.171 | -0.185 |
| Clinopyroxene | 0.060 | 0.054 | 0.041 | 0.027 | 0.014 | 0.001 | -0.012 | -0.027 | -0.041 | -0.057 | -0.074 | -0.091 | -0.108 | -0.125 | -0.141 | -0.156 | -0.171 | -0.185 |
| Olivine | 0.125 | 0.121 | 0.109 | 0.097 | 0.087 | 0.076 | 0.064 | 0.053 | 0.040 | 0.028 | 0.013 | -0.001 | -0.015 | -0.028 | -0.041 | -0.052 | -0.063 | -0.074 |
| Magnetite | 0.253 | 0.253 | 0.245 | 0.238 | 0.231 | 0.225 | 0.218 | 0.211 | 0.204 | 0.197 | 0.188 | 0.179 | 0.172 | 0.165 | 0.159 | 0.155 | 0.152 | 0.149 |
| Ilmenite | 0.125 | 0.121 | 0.109 | 0.097 | 0.087 | 0.076 | 0.065 | 0.053 | 0.042 | 0.030 | 0.016 | 0.003 | -0.010 | -0.022 | -0.034 | -0.044 | -0.054 | -0.062 |
| **Measured Data** | | | | | | | | | | | | | | | | | | |
| Sample name | B07-009 | B06-062 | B06-064 | B06-065 | B06-067 | | | B07-057 | B06-020* | B07-061 | B06-054 | B06-042 | B06-039 | B06-029 | B07-027 | B06-037 | B07-036 | B07-041 |
| Strat. height | 2210 | 2325 | 2495 | 2620 | 2775 | | | 3122 | 3260 | 3425 | 3634 | 3741 | 3925 | 4083 | 4232 | 4305 | 4460 | 4590 |
| % liquid equivalent | 99.74 | 95.70 | 89.74 | 85.35 | 79.91 | | | 67.74 | 62.89 | 57.11 | 49.77 | 46.02 | 39.56 | 34.02 | 28.79 | 26.23 | 20.79 | 16.23 |
| **Modes from LSQR Matlab (*VanTongeren et al.,* 2010)** | | | | | | | | | | | | | | | | | | |
| Plagioclase | 0.45 | 0.37 | 0.54 | 0.56 | 0.49 | NA | NA | 0.58 | 0.49 | 0.84 | 0.79 | 0.44 | 0.46 | 0.46 | 0.54 | 0.55 | 0.46 | 0.42 |
| Orthopyroxene | 0.31 | 0.49 | 0.21 | 0.22 | 0.23 | NA | NA | 0.14 | 0.19 | 0.06 | 0.00 | 0.00 | 0.00 | 0.00 | 0.00 | 0.00 | 0.00 | 0.00 |
| Clinopyroxene | 0.22 | 0.13 | 0.25 | 0.21 | 0.26 | NA | NA | 0.16 | 0.19 | 0.01 | 0.09 | 0.29 | 0.30 | 0.10 | 0.05 | 0.06 | 0.16 | 0.20 |
| Olivine | 0.00 | 0.00 | 0.00 | 0.00 | 0.00 | NA | NA | 0.00 | 0.00 | 0.00 | 0.05 | 0.17 | 0.12 | 0.24 | 0.23 | 0.22 | 0.24 | 0.19 |
| Magnetite | 0.00 | 0.00 | 0.00 | 0.00 | 0.00 | NA | NA | 0.08 | 0.09 | 0.04 | 0.04 | 0.03 | 0.06 | 0.07 | 0.07 | 0.07 | 0.00 | 0.02 |
| Ilmenite | 0.00 | 0.00 | 0.00 | 0.00 | 0.00 | NA | NA | 0.02 | 0.01 | 0.02 | 0.02 | 0.04 | 0.04 | 0.04 | 0.04 | 0.04 | 0.05 | 0.04 |
| **Modeled Whole Rock Fe Isotope Composition baesd on Observed Modes and Calculated Liquid Composition** | | | | | | | | | | | | | | | | | | |
| Whole Rock δ56Fe | 0.06 | 0.07 | 0.03 | 0.02 | 0.01 | NA | NA | 0.10 | 0.09 | 0.04 | 0.04 | 0.01 | 0.02 | 0.02 | 0.02 | 0.00 | -0.07 | -0.06 |

*This is the mode of B06-021.

**Table 2.** $\delta^{56}Fe$ values from whole rock and magnetite analyses with associated 2σ and lithology of the accompanying unit.

| Stratigraphic position relative to the Merensky Reef (m) | Sample Number | Latitude (S)[2] | Longitude (E)[2] | Equivalent % liquid remaining | $\delta^{56}Fe_{WR}$(‰) | 2σ | $\delta^{56}Fe_{magnetite}$ (‰)[1] | 2σ[1] | Lithology |
|---|---|---|---|---|---|---|---|---|---|
| 2210 | B07-009 | 24°51.778' | 29°58.114' | 99.74 | 0.06 | 0.09 | 0.61 | 0.06 | gabbro |
| 2325 | B06-062 | 24°51.778' | 30°01.770' | 95.70 | -0.15 | 0.07 | NA | NA | gabbro |
| 2495 | B06-064 | 24°51.851' | 30°01.842' | 89.74 | 0.06 | 0.04 | 0.69 | 0.08 | gabbro |
| 2620 | B06-065 | 24°51.858' | 30°01.565' | 85.35 | 0.19 | 0.13 | 0.65 | 0.08 | gabbro |
| 2775 | B06-067 | 24°51.917' | 30°01.398' | 79.91 | 0.09 | 0.07 | 0.47 | 0.11 | gabbro |
| 3122 | B07-057 | 24°48.985' | 29°58.275' | 67.74 | 0.15 | 0.08 | 0.86 | 0.07 | gabbro |
| 3260 | B06-020 | 24°48.974' | 29°58.149' | 62.89 | 0.12 | 0.07 | 0.34 | 0.03 | gabbro |
| 3425 | B07-061 | 24°48.914' | 29°57.798' | 57.11 | 0.16 | 0.07 | NA | NA | anorthosite |
| 3515 | B06-024 | 24°48.910' | 29°57.711' | 53.95 | 0.08 | 0.08 | 0.28 | 0.05 | troctolite |
| 3634 | B06-054 | 24° 48.763' | 29°57.186' | 49.77 | 0.07 | 0.08 | 0.53 | 0.06 | gabbro |
| 3741 | B06-042 | 24°48.776' | 29°57.036' | 46.02 | 0.08 | 0.05 | 0.61 | 0.04 | gabbro |
| 3925 | B06-039 | 24°48.857' | 29°56.833' | 39.56 | -0.01 | 0.03 | 0.59 | 0.04 | gabbro |
| 4083 | B06-029 | 24°48.895' | 29°56.650' | 34.02 | 0.08 | 0.05 | 0.37 | 0.07 | troctolite |
| 4232 | B07-027 | 24°49.072' | 29°56.433' | 28.79 | 0.21 | 0.09 | 0.35 | 0.09 | diorite |
| 4305 | B06-037 | 24°48.747' | 29°56.407' | 26.23 | 0.09 | 0.02 | 0.30 | 0.05 | diorite |
| 4355 | B06-055 | 24°51.874' | 29°54.756' | 24.47 | 0.12 | 0.06 | 0.38 | 0.02 | diorite |
| 4460 | B07-036 | 24°51.845' | 29°54.607' | 20.79 | 0.07 | 0.03 | 0.32 | 0.03 | diorite |
| 4508 | B07-037 | 24°51.827' | 29°54.550' | 19.11 | 0.16 | 0.05 | 0.63 | 0.17 | diorite |
| 4530 | B07-038 | 24°51.823' | 29°54.519' | 18.33 | 0.02 | 0.06 | 0.38 | 0.02 | diorite |
| 4555 | B07-039 | 24°51.800' | 29°54.488' | 17.46 | 0.18 | 0.04 | 0.63 | 0.05 | diorite |
| 4573 | B07-040 | 24°51.794' | 29°54.465' | 16.82 | 0.06 | 0.06 | 0.38 | 0.05 | diorite |
| 4590 | B07-041 | 24°51.829' | 29°54.430' | 16.23 | 0.07 | 0.03 | 0.56 | 0.03 | diorite |

[1]NA indicates that not enough pure magnetite could be separated from the sample for Fe isotope analysis.

[2]GPS coordinates form VanTongeren et al. (2010), VanTongeren and Mathez (2012) and VanTongeren and Mathez (2013).